Drying of thermally thick wood particles: A study of the numerical efficiency, accuracy and stability of common drying models

Inge Haberle,[*,†] Nils Erland L. Haugen,[†,‡] and Øyvind Skreiberg[‡]

[1]

†*Norwegian University of Science and Technology, Department of Energy and Process Engineering, Kolbjørn Hejes vei 1 B, 7491 Trondheim, Norway*

‡*SINTEF Energy Research, Department of Thermal Energy, Kolbjørn Hejes vei 1 A, 7491 Trondheim, Norway*

E-mail: inge.haberle@ntnu.no

Phone: +47 73 593697. Fax: -

Abstract

The primary focus of this paper is on studying different numerical models for drying of wet wood. More specifically, the advantages and disadvantages of the models with respect to numerical efficiency, stability and accuracy are investigated. The two basic models that are studied in detail are the thermal drying model and the kinetic rate drying model. The drying models have been implemented in an in-house simulation tool that solves for drying and devolatilization of a one-dimensional cylindrical wood log. It is found that the choice of drying model can significantly influence the computational time associated with the thermal conversion. Furthermore, the occurrence of numerical pressure oscillations in the thermal drying model has been found and investigated. The numerical oscillations are reduced by introducing an evaporation fraction, f_{evap}. When the thermal drying model is applied, the drying zone is very thin, commonly only including one grid point, which can result in numerical instabilities. The evaporation fraction allows the smearing of the drying zone by reducing the heat flux used for evaporation of liquid water and using the residual heat flux for heating up the grid points. Reducing the evaporation fraction also resulted in reduced CPU times. It was found that model accuracy was not significantly influenced by the choice of drying model.

Contents

Nomenclature

A	pre-exponential factor $[\frac{1}{\mathrm{s}}]$	$\triangle$h	heat of reaction $[\frac{\mathrm{kJ}}{\mathrm{kg}}]$
c_{P}	specific heat capacity $[\frac{\mathrm{J}}{\mathrm{kgK}}]$	h_{conv}	heat transfer coefficient $[\frac{\mathrm{W}}{\mathrm{m^2K}}]$
D_{b}	bound water diffusivity $[\frac{\mathrm{m}^2}{\mathrm{s}}]$	$h_{\mathrm{m,pore}}$	mass transfer coefficent of vapor in pores $[\frac{\mathrm{m}}{\mathrm{s}}]$
D_{eff}	effective mass diffusivity $[\frac{\mathrm{m}^2}{\mathrm{s}}]$	k	reaction rate constant $[\frac{1}{\mathrm{s}}]$
d_{P}	particle diameter [m]	M_{fsp}	moisture content at fiber saturation point; dry basis $[\frac{\mathrm{kg}}{\mathrm{kg}}]$
$d_{\mathrm{pore,hydraulic}}$	hydraulic pore diameter [m]	M_{l}	moisture content (liquid free water); dry basis $[\frac{\mathrm{kg}}{\mathrm{kg}}]$
E_a	activation energy $[\frac{\mathrm{kJ}}{\mathrm{mol}}]$		
f_{evap}	evaporation fraction [-]		

MW	molecular weight $[\frac{\text{kg}}{\text{mol}}]$
P_c	capillary pressure [Pa]
P_g	gas pressure [Pa]
P_l	liquid phase pressure [Pa]
R	ideal gas constant $[\frac{\text{kJ}}{\text{molK}}]$
r	radius [m]
T	temperature [K]
$S_{\text{C,wood}}$	specific surface area of wood $[\text{m}^2/\text{m}^3]$
t	time [s]
T_evap	boiling (evaporation) temperature [K]
u_r	gas phase velocity in radial direction $[\frac{\text{m}}{\text{s}}]$
u_l	liquid free water velocity in radial direction $[\frac{\text{m}}{\text{s}}]$
V	control volume $[\text{m}^3]$
Y	mass fraction [-]

Greek letters

α	Shrinkage parameter [-]
β	Shrinkage parameter [-]
γ	Shrinkage parameter [-]
ϵ_g	gas phase volume fraction [-]
ϵ_pore	porosity [-]
ϵ_particle	particle emissivity [-]
κ	permeability $[\text{m}^2]$
λ	thermal conductivity $[\frac{\text{W}}{\text{mK}}]$
μ	dynamic viscosity $[\frac{\text{kg}}{\text{sm}}]$
ρ	density $[\frac{\text{kg}}{\text{m}^3}]$
σ	Stefan-Boltzmann constant $[\frac{\text{W}}{\text{m}^2\text{K}^4}]$
ϕ	volume fraction of pores filled with water [-]
Φ	endothermic/ exothermic heat of reaction terms $[\frac{\text{J}}{\text{m}^3\text{s}}]$
$\dot{\omega}$	reaction rate $[\frac{\text{kg}}{\text{m}^3\text{s}}]$

Subscript

b	bound water
char	char

$devol, 1$	primary devolatilization
$devol, 2$	secondary devolatilization
eff	effective
i	reaction
ir	irreducible saturation
$evap$	evaporation
vap, corr	saturated water vapor mass fraction after re-condensation reactions
fsp	fiber saturation point
g,gas	total gas phase
k	gas species
l	liquid free water
$mix, total$	mixed gas phase
$recond.$	water vapor re-condensation reactions
$surf$	particle surface
tar	tar
$wall$	furnace wall
$wood$	dry wood
$wood, 0$	dry wood initial
$\parallel$	parallel to fiber direction
$\perp$	perpendicular to fiber direction
0	initial

Superscript

g	gas phase
sat	saturation

1 Introduction

Even though a significant amount of research has been focused towards numerical modeling of thermal conversion of thermally thick wet wood particles over the last decades,[1–7] little work has been done on numerical efficiency and accuracy of different drying models. The different drying models commonly applied when modeling drying of thermally thick wet wood particles, are the thermal, the kinetic rate and the equilibrium models. The kinetic rate model handles evaporation as a heterogeneous reaction that is described as an Arrhenius

expression, while the thermal model assumes drying to occur at 373 K and no further temperature increase in a grid cell is allowed unless all the water in a cell has been evaporated. The equilibrium model assumes that liquid water and water vapor are in thermodynamic equilibrium. As a consequence the evaporation rate is a function of the difference of equilibrium concentration and the actual water vapor concentration.[4] A focus on those drying models and their numerical efficiency is needed as this can support the development of a low computational-cost simulation tool describing thermal conversion of wood. The purpose of such a numerical model, describing thermal conversion of thermally thick wood particles and logs, can be its coupling to gas phase modeling (and therefore a CFD platform), such that the combined model can be used as a simulation tool for wood stove design and optimization.

Such an optimization of current wood stoves is needed due to stricter demands towards emissions, efficiency and user-friendliness in the future. So far improvements have mainly been achieved via experiments, while in contrast to this a combination of experiments and modeling can result in cost-efficient design developments for future wood stoves or other combustion units.[8] This highlights the need for detailed but also numerically efficient models describing thermal conversion of wood, which need to grant a high degree of flexibility, as both input fuel in a wood stove as well as boundary conditions of the solid phase model can vary significantly. This flexibility can only be achieved by multi-dimensional models, and in order to keep those models numerically efficient, it has to be known, which stage of the thermal conversion of wood is related to the highest computational cost and how this can be optimized. Studying numerical efficiency on a 1D model is a good basis for the extension of this model to a numerical efficient multi-dimensional model.

Besides the studies on numerical efficiency and accuracy, it is also important to develop a model that is not affected by numerical instabilities. Numerical oscillations related to the thermal drying model have already been observed but have only been discussed in a few papers, e.g. by Fatehi and Bai.[9] This lack of information on numerical instabilities of drying models leads to the motivation, that more research within this field is needed such that the

authors have added an additional discussion on numerical instabilities of drying models.

The progress in numerical modeling of these two stages of thermal conversion of wood is fast and a significant range of models and modeling approaches has been presented over the last years. A detailed discussion of those models for thermally thick particles is presented by Haberle et al.[10] Even though there is a number of works available discussing model development for drying and devolatilization, only very limited work has been done on studying numerical efficiency, accuracy and stability of drying models in detail.

2 Numerical modeling

A 1D mesh-based simulation tool for drying and devolatilization of an infinitely long wet cylindrical wood log was developed. The model solves for the solid phase, as well as the gas and liquid phase. The involved gas species are water vapor, non-condensable gases and tar. Intra-particle transportation of the gas phase was accounted for, while the intra-particle transportation of liquid water was neglected, even though it can theoretically also be activated in the model. Intra-particle transportation of liquid free water was activated and deactivated in two test cases, and it was found that the influence of intra-particle transportation of liquid water is negligible. As shown in the subsequent section, only one temperature equation is solved in the model. This is based on the assumption of thermal equilibrium between the phases. In earlier works regarding thermally thick particles it has been found that this assumption predicts conversion times to be by about 20% longer[11,12] compared to models based on individual temperature equations for the gas, solid and liquid phases. Still, a local thermal equilibrium was assumed in this model as it is assumed that by this simplification of the temperature equations, the efficiency of the model can be significantly increased while the accuracy is still acceptable. Drying was modeled by the thermal and the kinetic drying model. In addition the equilibrium model was also partly tested. Devolatilization was described by a three independent competitive reactions scheme and secondary tar

reactions (see Figure 1).

$$\text{Dry wood} \begin{cases} \xrightarrow{k1} \text{Non} - \text{condensable gases} \\ \xrightarrow{k2} \text{Tar} \\ \xrightarrow{k3} \text{Char} \end{cases}$$

$$\text{Tar} \begin{cases} \xrightarrow{k4} \text{Non} - \text{condensable gases} \\ \xrightarrow{k5} \text{Char} \end{cases}$$

Figure 1: Three independent competitive reactions scheme in combination with the secondary tar reactions.

The governing equations require simplifications in order to be able to simultaneously describe all chemical reactions and physical phenomena related to thermal wood conversion at reasonable computational cost.

The applied simplifying assumptions are:

1. Darcy's law can be used for modeling the gas phase flow in the wood particle. Hereby, one does not have to solve the momentum equation, which reduces the computational cost of the model. The accuracy is assumed to not be affected by this assumption, as it is known that, with respect to increasing particle sizes, the convective term in the transport equations becomes less important.[13] In this work, only thermally thick particles are modeled, which as such are related to larger particle sizes.

2. The gases in the solid matrix are assumed to be ideal. As reviewing a number of models has shown, such an assumption is common practice in thermal wood particle conversion modeling.[10]

3. The blowing effect of the leaving volatiles on heat and mass transfer to the particle is neglected. It is assumed that radiation dominates over convection with respect to heat transfer to the particle, which makes the effect of blowing on the heat transfer

negligible. Furthermore, since char conversion is not included, the mass transfer to the particle surface from the surrounding gas is irrelevant.

4. During drying, shrinkage is neglected as it is small compared to shrinkage during devolatilization.[4] Shrinkage during devolatilization is considered by a three-parameter model, which is based on constant shrinkage parameters (α, β and γ). A more detailed description of this shrinkage model and a detailed discussion of the three different shrinkage parameters can be found elsewhere.[14] This simplifies the complexity of shrinkage modeling and reduces computational cost.

5. Cracking and fragmentation are neglected. This results in reduced computational cost. Neglecting these structural changes might affect model accuracy, as they will affect the permeability of the particle and therefore the flow of the exiting gas phase.

6. The model is 1D, which reduces the computational cost significantly. For investigation of fundamental processes, it is assumed that this is a valid approach. Furthermore, it is assumed that an optimized 1D model is a good starting point for extension to 2D or 3D.

7. A bridge factor is implemented to account for anisotropy, since this is the only way anisotropy can be considered in 1D models. However, a bridge-factor-consideration of the anisotropic wood simplifies anisotropy significantly. For accurate anisotropy consideration multi-dimensional models are required.

8. Most of the thermo-physical properties are modeled as linearly dependent on the degree of conversion and/or temperature, e.g. permeability, thermal conductivity, specific heat capacity; commonly a temperature increase is related to an increase of those values. This consideration is assumed to lead to higher accuracy of the model compared to the assumption of constant thermo-physical properties. Furthermore, the implementation of linear functions of the properties is assumed to not significantly contribute to an

increasing complexity of the model.

9. Tar re-condensation reactions have been neglected. It is assumed that these reactions occur only to a negligible extent.

The model validation was done against experimental work by Lu et al.[5] Good agreement between the modeling predictions and the experiments was found.

2.1 Governing equations

The gas phase continuity equation is given by[15]

$$\frac{\partial \epsilon_{\mathrm{g}} \rho_{\mathrm{g}}^{\mathrm{g}}}{\partial t} + \frac{1}{r}\frac{\partial (r \rho_{\mathrm{g}}^{\mathrm{g}} \epsilon_{\mathrm{g}} u_{\mathrm{r}})}{\partial r} = \dot{\omega}_{\mathrm{gas}} - \frac{\rho_{\mathrm{g}}^{\mathrm{g}} \epsilon_{\mathrm{g}}}{V}\frac{\partial V}{\partial t} \tag{1}$$

where $\rho_{\mathrm{g}}^{\mathrm{g}}$ is the intrinsic phase average of the total gas phase density, ϵ_{g} is the volume fraction occupied by the gas phase, u_{r} is the superficial gas phase velocity in radial direction, r is the radius, V is the cell volume related to one grid point in the 1D mesh and $\dot{\omega}_{\mathrm{gas}}$ is the reaction rate due to evaporation and devolatilization. The volume fraction occupied by the gas phase can be calulated from the porosity, ϵ_{pore}, according to

$$\epsilon_{\mathrm{g}} = \epsilon_{\mathrm{pore}}(1 - \phi) \tag{2}$$

with ϕ being the fraction of pores that is filled with water and ϵ_{pore} is equal to V_{pore}/V. The gas phase contains water vapor, tar, non-condensable gases and air. A simplified consideration of air, instead of explicit modeling of nitrogen and oxygen, is valid as long as oxygen consuming reactions are not relevant. The last term in Eq. (1) represents the shrinkage, and similar expressions in Eq. (7), Eq. (8) and Eq. (9) refer to the same structural change. In

case of wood drying and devolatilization, $\dot{\omega}_{\text{gas}}$ is expressed as

$$\begin{aligned}\dot{\omega}_{\text{gas}} = (k_1 + k_2)\rho_{\text{wood}} - k_5\rho^{\text{g}}_{\text{tar}}\epsilon_{\text{g}} \\ +\dot{\omega}_{\text{evap}} - \dot{\omega}_{\text{recond.,l}}\end{aligned} \tag{3}$$

where $\dot{\omega}_{\text{evap}}$ is the source term due to evaporation of liquid free water and bound water, while $\dot{\omega}_{\text{recond.,l}}$ models the re-condensation of water vapor to liquid free water.

The reaction rate constants in Eq. (3) are calculated according to the Arrhenius expression

$$k_i = A_i \exp\left(\frac{-E_{\text{a,i}}}{RT}\right) \tag{4}$$

for devolatilization reactions with R being the ideal gas constant and T the temperature. The superficial gas phase velocity, u_{r}, is described by Darcy's law[15]

$$u_{\text{r}} = \frac{-\kappa}{\mu_{\text{g}}}\frac{\partial P_{\text{g}}}{\partial r}, \tag{5}$$

where μ_{g} is the dynamic viscosity of the gas phase and κ is the permeability of the solid.

The gas phase pressure can be obtained from the gas phase density by using the ideal equation of state

$$P_{\text{g}} = \frac{\rho^{\text{g}}_{\text{g}} RT}{MW_{\text{mix,total}}} \tag{6}$$

with $MW_{\text{mix,total}}$ being the total mixed molecular weight.

The gas species evolution equation is given by[15]

$$\begin{aligned}\frac{\partial(\epsilon_{\text{g}}\rho^{\text{g}}_{\text{g}}Y_k)}{\partial t} + \frac{1}{r}\frac{\partial(r\rho^{\text{g}}_{\text{g}}\epsilon_{\text{g}}Y_{\text{k}}u_{\text{r}})}{\partial r} \\ = \frac{1}{r}\frac{\partial}{\partial r}\left(r\epsilon_{\text{g}}\rho^{\text{g}}_{\text{g}}D_{\text{eff}}\frac{\partial Y_{\text{k}}}{\partial r}\right) - \frac{\epsilon_{\text{g}}\rho^{\text{g}}_{\text{g}}Y_{\text{k}}}{V}\frac{\partial V}{\partial t} + \dot{\omega}_k\end{aligned} \tag{7}$$

where D_{eff} is the effective diffusivity and Y_k is the mass fraction of species k, which could be either tar, non-condensable gases or water vapor since the mass fraction of air is calculated

by difference. The evolution of the mass density of wood reads[15]

$$\frac{\partial \rho_{\text{wood}}}{\partial t} = -(k_1 + k_2 + k_3)\rho_{\text{wood}} - \frac{\rho_{\text{wood}}}{V}\frac{\partial V}{\partial t}, \tag{8}$$

and the evolution equation for char mass density is given as

$$\frac{\partial \rho_{\text{char}}}{\partial t} = k_3 \rho_{\text{wood}} + \epsilon_{\text{g}} k_5 \rho_{\text{tar}}^{\text{g}} - \frac{\rho_{\text{char}}}{V}\frac{\partial V}{\partial t}. \tag{9}$$

The temperature equation reads[16]

$$\begin{aligned} \Big(\rho_{\text{wood}} c_{P,\text{wood}} + \rho_{\text{char}} c_{P,\text{char}} + \rho_{\text{l}} c_{P,\text{l}} + \rho_{\text{b}} c_{P,\text{b}} + \epsilon_{\text{g}} \rho_{\text{g}}^{\text{g}} c_{P,\text{g}}\Big)\frac{\partial T}{\partial t} + \\ \Big(\rho_{\text{l}} c_{\text{P,l}} u_{\text{l}} + \rho_{\text{b}} c_{\text{P,b}} u_{\text{b}} + \rho_{\text{g}}^{\text{g}} \epsilon_{\text{g}} c_{\text{P,g}} u_{\text{r}}\Big)\frac{\partial T}{\partial r} = \frac{1}{r}\frac{\partial}{\partial r}\Big(r \lambda_{\text{eff}}\Big(\frac{\partial T}{\partial r}\Big)\Big) - \Phi_{\text{evap}} - \Phi_{\text{devol,1}} + \Phi_{\text{devol,2}}, \end{aligned} \tag{10}$$

where the source term Φ_{evap} refers to the endothermicity of evaporation reactions; $\Phi_{\text{devol,1}}$ represents the source terms related to primary devolatilization reactions, commonly modeled as endothermic, and $\Phi_{\text{devol,2}}$ are exothermic secondary tar reactions. However, the definition of the heat of reaction for primary and secondary devolatilization reactions is still a challenge, since the experimental determination is difficult.[17–20] Furthermore it has to be pointed out that $\rho_{\text{g}}^{\text{g}}$ refers to the intrinsic gas phase average, while ρ_{g} refers to the gas phase average. The relationship between the two densities is given by

$$\rho_{\text{g}} = \rho_{\text{g}}^{\text{g}} \epsilon_{\text{pore}} (1 - \phi). \tag{11}$$

The particle surface temperature is dependent on the radiative influx from the wall and the convective heat transfer to the particle surface, such that the heat flux to the surface is given by

$$\begin{aligned} \lambda_{\text{eff}}\frac{\partial T}{\partial r} = \sigma \epsilon_{\text{particle}}(T_{\text{wall}}^4 - T_{\text{surf}}^4) \\ + h_{\text{conv}}(T_{\text{gas}} - T_{\text{surf}}), \end{aligned} \tag{12}$$

where σ is the Stefan-Boltzmann-constant, h_{conv} is the heat transfer coefficient, $\epsilon_{\mathrm{particle}}$ is the emissivity of the particle and λ_{eff} is the effective thermal conductivity of the outer part of the particle.

Mass conservation of liquid free water is calculated as[21]

$$\frac{\partial \rho_{\mathrm{l}}}{\partial t} + \frac{1}{r}\frac{\partial\Big(r\rho_{\mathrm{l}}u_{\mathrm{l}}\Big)}{\partial r} = -\dot{\omega}_{\mathrm{evap,l}} + \dot{\omega}_{\mathrm{recond.,l}} \tag{13}$$

where the velocity of the liquid free water is calculated according to

$$u_{\mathrm{l}} = -\frac{\kappa_{\mathrm{l}}}{\mu_{\mathrm{l}}}\frac{\partial P_{\mathrm{l}}}{\partial r} \tag{14}$$

where μ_{l} is the dynamic viscosity of the liquid phase, κ_{l} is the permeability of the liquid water and ρ_{l} is defined as

$$\rho_{\mathrm{l}} = \rho_{\mathrm{l}}^{\mathrm{l}}\phi\epsilon_{\mathrm{pore}} \tag{15}$$

with ϕ being the volume fraction of pores filled with water and $\rho_{\mathrm{l}}^{\mathrm{l}}$ is the intrinsic density of water (1000 kg/m^3). The pressure of the liquid phase, P_{l}, is calculated as[21]

$$P_{\mathrm{l}} = P_{\mathrm{g}} - P_{\mathrm{c}}, \tag{16}$$

and the capillary pressure P_{c} is calculated according to[22]

$$P_{\mathrm{c}} = 10000\Big(\frac{\rho_{\mathrm{wood,0}}M_{\mathrm{l}}}{\epsilon_{\mathrm{pore}}\rho_{\mathrm{l}}}\Big)^{-0.61} \tag{17}$$

where M_{l} is the mass fraction of liquid free water (on dry basis). This correlation and the applied coefficients were suggested by Spolek and Plumb,[23] who presented this equation after having measured the capillarity pressure of pine wood. Regarding the water vapor re-condensation reactions it is assumed that the water vapor re-condensation reactions, $\dot{\omega}_{\mathrm{recond.,l}}$,

can be modeled by an equilibrium assumption[5]

$$\dot{\omega}_{\text{recond.,l}} = S_{\text{C,wood}} \frac{\rho_{\text{l}}}{\rho_{\text{l,0}}} h_{\text{m,pore}} \epsilon_{\text{g}} \left(\rho_{\text{v}}^{\text{sat}} - Y_{\text{vap}} \rho_{\text{g}}^{\text{g}} \right) \tag{18}$$

with $S_{\text{C,wood}}$ being the specific surface area of wood and $\rho_{\text{l,0}}$ is the initial liquid free water density. The initial liquid free water density is defined as the water density in the wood log before drying has started. The mass transfer coefficient of vapor in the pore, $h_{\text{m,pore}}$, is defined as[5]

$$h_{\text{m,pore}} = 3.66 D_{\text{eff,fw}} / d_{\text{pore,hydraulic}}, \tag{19}$$

while the hydraulic pore diameter is[5]

$$d_{\text{pore,hydraulic}} = \frac{4\epsilon_{\text{pore}}}{S_{\text{C,wood}}(1 - \epsilon_{\text{pore}})} \tag{20}$$

and the effective liquid free water diffusivity is[5]

$$D_{\text{eff,fw}} = 6.1 \times 10^3 \left(\frac{\kappa_{\text{l}}}{\mu_{\text{l}}} \right) \epsilon_{\text{pore}}^{0.61} \left(\frac{\rho_{\text{wood}} M_{\text{l}}}{\rho_{\text{l}}} \right). \tag{21}$$

The liquid permeability κ_{l} is given as[5]

$$\kappa_{\text{l}} = \begin{cases} 0, & \text{if } \left(\frac{\rho_{\text{wood}} \text{M}_{\text{l}}}{\epsilon_{\text{pore}} \rho_{\text{l}}}\right) \leq S_{\text{ir}} \\ \kappa_{\text{l}}^{\Phi} \left(1 - \cos \frac{\pi}{2} \left(\frac{\frac{\rho_{\text{wood}} M_{\text{l}}}{\epsilon_{\text{pore}} \rho_{\text{l}}} - S_{\text{ir}}}{1 - S_{\text{ir}}} \right) \right), & \text{if } \left(\frac{\rho_{\text{wood}} \text{M}_{\text{l}}}{\epsilon_{\text{pore}} \rho_{\text{l}}}\right) > S_{\text{ir}} \end{cases}$$

when $S_{\text{ir}} = 0.1$ being the irreducible saturation and $\kappa_{\text{l}}^{\Phi} = 3 \times 10^{-15}$ m^2.[5] The equation for κ_{l} was used by de Paiva Souza[22] who referred to experimental work by Tesoro et al.[24] The coefficients in Eq. (21) can be traced back to the previously mentioned definition of capillary pressure. The diffusivity that is required here is defined by expressing the liquid free water flux by Darcy's law and re-formulate this flux and expressing it by Fick's law.

The liquid viscosity μ_{l} is defined as[22]

$$\log(\mu_{\mathrm{l}}) = -13.73 + \frac{1828}{T} + 1.966 \times 10^{-2} T \\ -1.466 \times 10^{\cdot -5} T^2 \tag{22}$$

in order to correctly describe the temperature dependency of liquid viscosity. The saturated vapor pressure is calculated as[21]

$$P_{\mathrm{vap}}^{\mathrm{sat}} = \exp\Big(24.1201 - 4671.3545/T\Big) \tag{23}$$

and the corresponding water vapor density is calculated according to

$$\rho_{\mathrm{v}}^{\mathrm{sat}} = \frac{P_{\mathrm{vap}}^{\mathrm{sat}} MW_{\mathrm{water}}}{RT}. \tag{24}$$

The equation for saturated water vapor pressure has been obtained from fitting the expression to water vapor data over a flat plate.[25]

Mass conservation of bound water, ρ_{b}, is calculated according to[21]

$$\frac{\partial \rho_{\mathrm{b}}}{\partial t} = \frac{1}{r}\frac{\partial}{\partial r}\Big(r D_{\mathrm{b}} \frac{\partial \rho_{\mathrm{b}}}{\partial r}\Big) - \dot{\omega}_{\mathrm{evap,b}} \tag{25}$$

when the density of dry wood is assumed to be constant since no organic mass is converted during drying. In the equation above, D_{b} is the bound water diffusivity. The bound water diffusivity in tangential direction is calculated based on the equation discussed by Grønli[21]

$$D_{\mathrm{b}} = 7 \times 10^{-6} \exp\Big(\frac{-4633 + 3523 \frac{\rho_{\mathrm{b}}}{\rho_{\mathrm{wood}}}}{T}\Big) \tag{26}$$

and the one in radial direction is obtained by multiplying the tangential one by 2/3 as suggested by Grønli.[21] This expression for bound water diffusivity, including all the coefficients, has been derived by Siau,[26] and is based on experimental work by Stamm.[27]

Based on all the previously discussed equations, the time integrator must be able to handle a system of differential and algebraic equations.[21] Therefore, the IDA solver, included in SUNDIALS[28] was applied. It uses a backward differentiation formula.

2.2 Drying

There are three different drying models that are commonly discussed in the literature; the thermal model, the kinetic rate drying model and the equilibrium model.[4] In this work, only the thermal model, the kinetic rate model or a combination of the two drying models, are tested in detail. The equilibrium model is not included in the discussion of numerical efficiency and stability, as it is commonly applied only for low-temperature drying processes.[4,29] However, it was also implemented, to see if its results are more similar to the results of the kinetic rate model or the thermal model.

For implementation of the equilibrium model the mass fraction of water vapor, $Y_{\text{vap,corr}}$, due to the change in saturated vapor pressure is calculated according to

$$Y_{\text{vap,corr}} = \frac{P_{\text{vap}}^{\text{sat}}}{P_{\text{g}}} \frac{MW_{\text{water}}}{MW_{\text{mix,total}}} \tag{27}$$

where $P_{\text{vap}}^{\text{sat}}$ is defined in Eq. (23) and the evaporation rate is then calculated as

$$\dot{\omega}_{\text{evap}} = -\frac{\epsilon_{\text{pore}}(1-\phi)\rho_{\text{g}}^{\text{g}}(Y_{\text{vap,corr}} - Y_{\text{vap}})}{dt} \tag{28}$$

where dt is the time step size, ϵ_{pore} is again the porosity and Y_{vap} is the mass fraction of water vapor at the old time step.

The thermal drying model is based on the concept of actively switching on and off the evaporation in a grid cell. Mathematically, this relation can be expressed as[9]

$$\dot{\omega}_{\text{evap}} = \begin{cases} -f_{\text{evap}} \frac{F_{\text{heat}}}{\triangle h_{\text{evap}}}, & T \geq T_{\text{evap}}, \rho_l > 0 \\ 0, & \text{otherwise} \end{cases} \tag{29}$$

where $\dot{\omega}_{\text{evap}}$ is the evaporation rate, and f_{evap} is the evaporation fraction and the heat flux, F_{heat}, is given by

$$F_{\text{heat}} = \frac{1}{r}\frac{\partial}{\partial r}\Big(r\epsilon_{\text{pore}}(1-\phi)\rho_{\text{g}}^{\text{g}}u_{\text{r}}c_{\text{P,g}}T - r\lambda_{\text{eff}}\frac{\partial T}{\partial r}\Big). \tag{30}$$

The thermal drying model is commonly based on the assumption that drying occurs at a fixed boiling temperature of 373 K.[4] In this work, evaporation temperature and boiling temperature are used interchangeably. However, during drying, a significant amount of water suddenly evaporates and enters the gas phase as water vapor, which results in pressure increase. The pressure in the interior of the wood particle may therefore significantly differ from atmospheric pressure. Such a higher internal pressure results in increased evaporation temperatures, which yield liquid free water evaporation above 373 K. In order to account for this, the evaporation temperature is modeled as a function of the internal pressure according to

$$T_{\text{evap}} = T_A \log(P_{\text{g}}/P_{\text{1atm}}) + T_0, \tag{31}$$

when $T_A = 32.7$ K, $T_0 = 373$ K and $P_{\text{1atm}} = 101325$ Pa. The coefficients within this equation have been determined by calculating the temperature from a given saturated water vapor internal pressure and fitting a mathematical expression to this correlation.

This pressure-dependent boiling temperature can only be applied in a model that accurately monitors pressure evolution inside the wood particle.

The kinetic rate drying model describes drying as a chemical reaction, which can be expressed by an Arrhenius term

$$\dot{\omega}_{\text{evap}} = k_{\text{evap}}\rho_{\text{water}} \tag{32}$$

where ρ_{water} is the density of the liquid water. In this work only bound water evaporates according to the kinetic rate drying model, such that bound water density substitutes for liquid water density in the previous equation. The evaporation rate constant is expressed as[30]

$$k_{\text{evap}} = A_{\text{evap}} \exp\Big(\frac{-E_{\text{a,evap}}}{RT}\Big). \tag{33}$$

In the literature, a broad range of different kinetics is used to describe evaporation, with the most common ones listed in Table 1.

Table 1: Kinetic data for the kinetic rate drying model. [1)] indicates that the first value is used for liquid free water evaporation modeling and the second term is used for bound water evaporation modeling.

Activation energy [kJ/mol]	Pre-exponential factor [1/s]	Reference
88	5.13×10^{10}	[9,30]
24 / 120 [1)]	5.13×10^{6}	[31]
88	5.60×10^{8}	[32]
88	5.13×10^{6}	[33]

The wide range of different kinetic data used to model drying suggests that the drying model is commonly tuned in order to fit experimental data. In this model the first and the third set of kinetic data have been tested. The main advantage of the kinetic rate drying model is that it is more numerically stable[4] than the thermal drying model.

It is also possible to model drying with a combination of the thermal model and the kinetic rate model. In such a case, the evaporation of the liquid free water is modeled with the thermal model and the evaporation of the bound water is described by the kinetic rate model. The critical moisture content, which defines whether liquid free water or bound water need to be modeled, is the fiber saturation point M_{fsp}, which is commonly set to 30 wt% on oven-dry basis.

2.3 Devolatilization

Devolatilization, see Table 2, is described by three independent competitive reactions scheme, where wood degrades to the main products; tar, char and non-condensable gases.[21] After the primary devolatilization, tar reacts further, commonly via intra-particle cracking and re-polymerization reactions, and forms non-condensable gases and char, respectively.[15] The kinetic data for primary and secondary devolatilization reactions was taken from Lu et al.[5]

Table 2: Kinetic data used for modeling devolatilization, which are the same as in Lu et al.[5] *"Gases"* in the following table refer to non-condensable gases. [1)] marks that the heat of reaction for primary devolatilization reactions was taken specifically for poplar and was therefore not taken from Lu et al.[5]

Reaction rate constant	Reaction	Pre-exponential factor [1/s]	Activation energy [kJ/mol]	Ref.	Heat of reaction [kJ/kg]	Ref.
k_1	Wood → Gases	1.11×10^{11}	177	[34]	-207[1)]	[18]
k_2	Wood → Tar	9.28×10^{9}	149	[34]	-207[1)]	[18]
k_3	Wood → Char	3.05×10^{7}	125	[34]	-207[1)]	[18]
k_4	Tar → Gases	4.28×10^{6}	107.5	[35]	42	[36]
k_5	Tar → Char	1×10^{5}	107.5	[37]	42	[36]

Devolatilization is a complex process where both chemical and physical processes influence each other, and therefore have to be considered simultaneously. The influence of extractives on chemical reactions has not been explicitly considered, since wood is already modeled as a mixture of compounds.

3 Numerical setup

In the cases presented in this paper, the following case-specific boundary conditions and additional settings of the 1D simulation tool were used:

1. The furnace wall and gas phase temperatures were set to 1276 K and 1050 K, respectively.[5]
2. The pressure at the particle surface was set equal to the ambient pressure.
3. The boundary condition for the species mass fractions was a zero-gradient condition.
4. The 1D mesh includes 55 grid points along the whole particle diameter. The particle radius is therefore devided into an equidistant grid by 27 grid points.
5. The convective terms were discretized by first-order upwinding.
6. Diffusive terms were discretized by central differencing.

7. The maximum time step was 10^{-5} s.

8. Mass conservation was checked for 55 as well as 111 grid points. For the test run with 55 grid points, the relative error was 2.6%, while for 111 the relative error was 2.15%.

It was found that with 55 grid points a grid independent solution is obtained. The wood properties used in the model are listed in Table 3.

Table 3: Properties used as input values for the drying and devolatilization model. The data is applied for poplar wood (hardwood).

Property	Unit	Value	Reference
Apparent wood density, ρ_{wood}	[kg/m^3]	570	1)
True wood density, $\rho_{\text{wood, true}}$	[kg/m^3]	1500	38
Porosity, $\epsilon_{\text{pore,0}}$	[-]	0.62	1)
Thermal conductivity (wood), $\lambda_{\text{wood},\parallel}$	[W/(mK)]	$0.291 + 2.7588\times 10^{-4}$ T	39
Thermal conductivity (wood), $\lambda_{\text{wood},\perp}$	[W/(mK)]	$\frac{\lambda_{\text{wood},\parallel}}{1.9}$	39
Thermal conductivity (char), $\lambda_{\text{char},\parallel,\perp}$	[W/(mK)]	0.071	5
Thermal conductivity (gases), λ_{g}	[W/(mK)]	25.77×10^{-3}	5
Bridge factor, ξ	[-]	0.68	15
Specific heat capacity (wood), $c_{\text{P, wood}}$	[J/(kgK)]	1500 + T	4
Specific heat capacity (char), $c_{\text{P, char}}$	[J/(kgK)]	$420 + 2.09$ T $+ 6.85 \times 10^{-4}$T^2	4
Specific heat capacity (gases), $c_{\text{P, g}}$	[J/(kgK)]	1100	14
Dynamic viscosity (gases), μ_{gases}	[kg/(ms)]	3×10^{-5}	14
Diffusivity, D_{eff}	[m^2/s]	1×10^{-8}	2)
Permeability of wood, $\kappa_{\text{wood }\perp,\parallel}$	m^2	1×10^{-14}	40
Permeability of char, $\kappa_{\text{char }\perp,\parallel}$	m^2	1×10^{-13}	41
Permeability for liquid phase, κ_{l}	m^2	0	3)
Shrinkage parameters, $\alpha/\ \beta/\ \gamma$	[-]	1/0.75/1	4)
Latent heat of evaporation, $\triangle h_{\text{evap}}$	[J/kg]	2.44×10^6	5
Particle emissivity $\epsilon_{\text{particle}}$	[-]	0.7	3)
Particle diameter, d_{P}	[m]	9.5×10^{-3}	5
Aspect ratio	[-]	4	5
Moisture content	[wt% wet basis]	40	5
Specific surface area of wood	[m^2/m^3]	9.04×10^4	5

1) marks that this value was calculated based on knowing the apparent density and the true density.

2) outlines that this value was assumed to avoid tar diffusion and therefore re-condensation in inferior grid points.

3) marks that this value was assumed by the authors.

4) indicates that the shrinkage parameters were assumed by the authors for fitting modeling results.

The apparent wood density deviates slightly from what Lu et al.[5] and Mehrabian et al.[4] used, which is due to the fact that we chose the porosity such that the apparent wood density can be derived from the true wood density according to

$$\rho_{\text{wood,apparent}} = \rho_{\text{wood,true}}(1 - \epsilon_{\text{pore}}). \tag{34}$$

However, this density difference is minor.

4 Results and discussion

Different permeabilities of the liquid water were tested. The effective permeability, which was obtained via

$$\kappa_{\text{l,eff}} = \kappa_{\text{l,relative}}\kappa_{\text{l,intrinsic}}. \tag{35}$$

where $\kappa_{\text{l,intrinsic}}$ is the intrinsic liquid permeability, defined as[21]

$$\kappa_{\text{l,intrinsic}} = \kappa_{\text{g,dry wood}}. \tag{36}$$

This suggests that the intrinsic permeability of liquid water is equal to the one for the gas mixture. The effective permeability of the liquid phase is plotted in Figure 2.

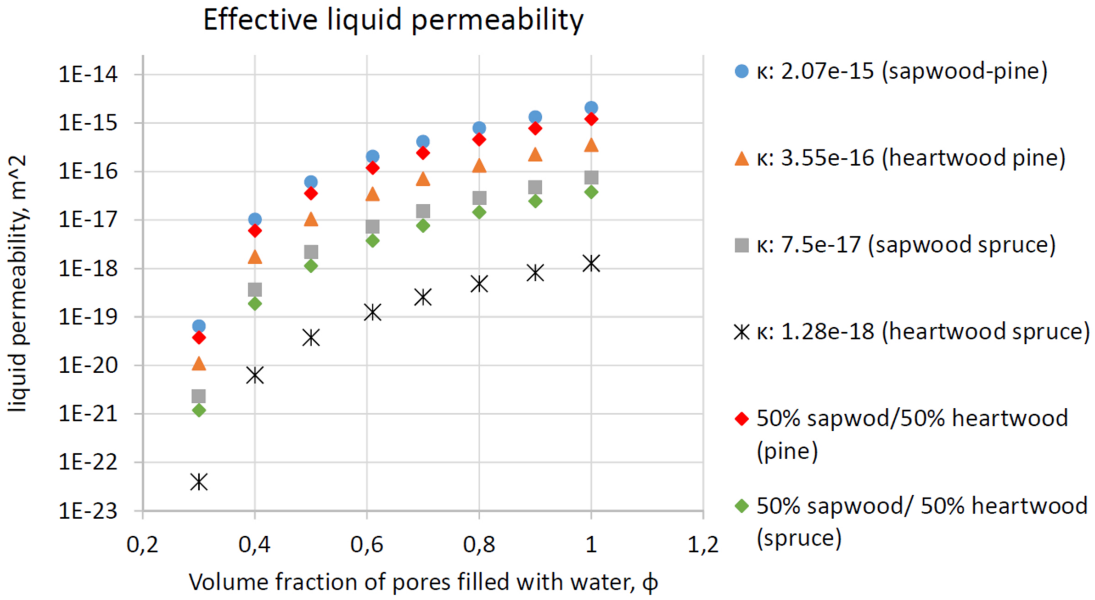

Figure 2: Comparison of effective liquid permeabilities for spruce and pine. The effective liquid permeability is plotted against the volume fraction of pores filled with water. The effective liquid permeability is defined as $\kappa_{\mathrm{l,eff}} = \kappa_{\mathrm{l,relative}}\kappa_{\mathrm{l,intrinsic}}$, where the definitions of $\kappa_{\mathrm{l,relative}}$ and $\kappa_{\mathrm{l,intrinsic}}$ (mentioned as κ in the plot) have been taken from Grønli.[21] For the definition of the relative permeability the initial porosity, $\epsilon_{\mathrm{pore},0}$=0.62, (as assumed in this work) and therefore a dry wood density of 570 kg/m^3 were used.

387 The water saturation S is defined as[21]

$$S = \frac{M - M_{\mathrm{fsp}}}{M_{\mathrm{sat}} - M_{\mathrm{fsp}}} \tag{37}$$

388 where M_{fsp}, M and M_{sat} are the fiber saturation point (set to 0.3), the actual liquid water
389 fraction and the water fraction at saturation. The water saturation has to be known to
390 define the relative permeability in longitudinal direction, such that

$$\kappa_{\mathrm{l,relative,long}} = S^8 \tag{38}$$

391 and

$$\kappa_{\mathrm{l,relative,tang}} = S^3 \tag{39}$$

392 if the permeability in tangential direction is to be defined.

393 Since there is commonly very little difference between radial and tangential directions,
394 the authors have assumed that

$$\kappa_{\mathrm{l,relative,tang}} = \kappa_{\mathrm{l,relative,rad}} \tag{40}$$

395 with $\kappa_{\mathrm{l,relative,rad}}$ being the relative liquid permeabilities in radial direction. In Figure 2 it is
396 shown that for volume fractions of pores filled with water smaller than 0.5, which are within
397 a typical range for wood burned in wood stoves, the liquid permeability is commonly below
398 1×10^{-16} m^2. The liquid permeabilities plotted in Figure 2 are valid for softwoods. Due to
399 lower porosities (and consequently higher dry virgin wood densities) hardwood species, such
400 as poplar, which is modeled in this work, will have even lower liquid permeabilities compared
401 to the softwood species.

402 The influence of the liquid permeability on the modeling results is plotted in Figure 3a
403 and Figure 3b.

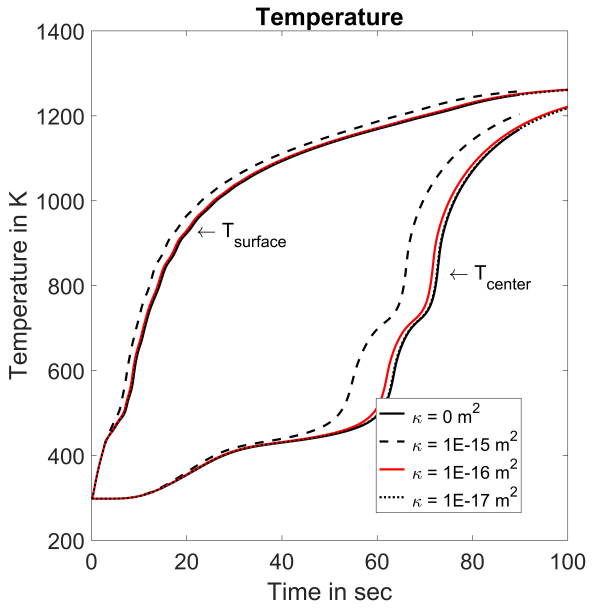

(a) Influence of choice of liquid permeability on center and surface temperature predictions.

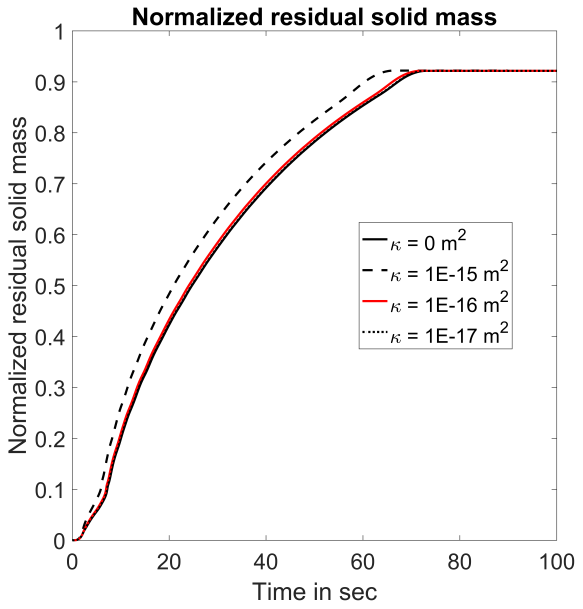

(b) Influence of choice of liquid permeability on normalized residual solid mass predictions.

Figure 3: Determination of the relevance of liquid water convection modeling. Liquid water convection is fully neglected when the liquid permeability is set to 0 m^2. The orders of magnitude of the other tested liquid permeabilities have been taken from literature.[21] (For distinct differentiation of the plotted lines see the online version of this article.)

It was found that only a liquid permeability as high as 10^{-15} m^2 yielded significantly different results compared to fully neglecting the liquid water convection. Liquid permeabilities of the order of 10^{-16} m^2 and 10^{-17} m^2 did not significantly differ from the assumption of fully negligible liquid water convection.

Based on Figure 3 one can justify that a typical effective liquid permeability of 10^{-16} m^2 (or smaller) can be used for modeling liquid water convection in wood particles or logs burning in wood stoves. Since the corresponding results are very similar to the results of a model that is fully neglecting liquid water convection, one can as well simplify the thermal conversion model of a wood particle by fully neglecting liquid water convection.

The focus on permeability of liquid water with respect to its influence on the model, was due to the numerical instabilities a non-zero and comparably large permeability can result in when applied together with the thermal drying model. These instabilities are due to

continuous on- and off-switching of evaporation reactions in cells where drying has already been fully accomplished at an earlier time. This re-activation of drying is due to some liquid water transportation outwards to dry cells and the requirement that whatever water present there has to be gone if temperatures shall exceed the boiling temperature.

The authors' conclusion was therefore, that liquid permeability can be set to zero and convective liquid free water transportation can be neglected, since this does not affect modeling results while at the same time it can stop the numerical instabilities.

As mentioned earlier, the authors have also tested the equilibrium model in order to see, whether its results were more similar to predictions obtained from the thermal drying model or the kinetic rate drying model. It was found that the equilibrium model, would predict a significantly different center temperature compared to the thermal drying model and the kinetic rate drying model with a lower pre-exponential factor (see Figure 4).

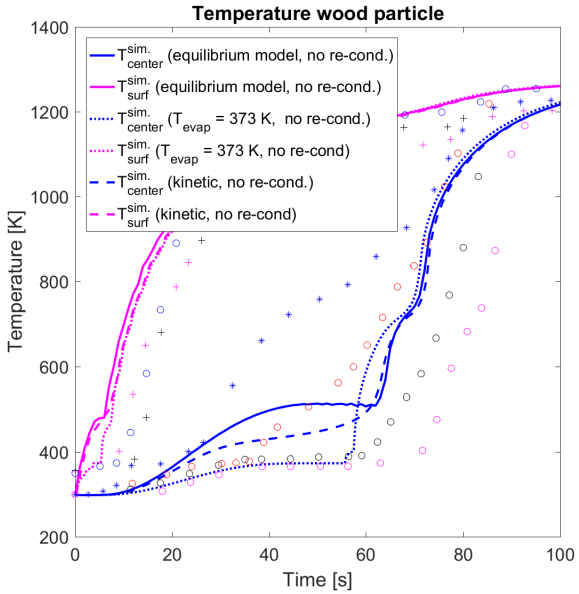

(a) Comparison of the center and surface temperature predicted with the thermal, the kinetic rate and the equilibrium model.

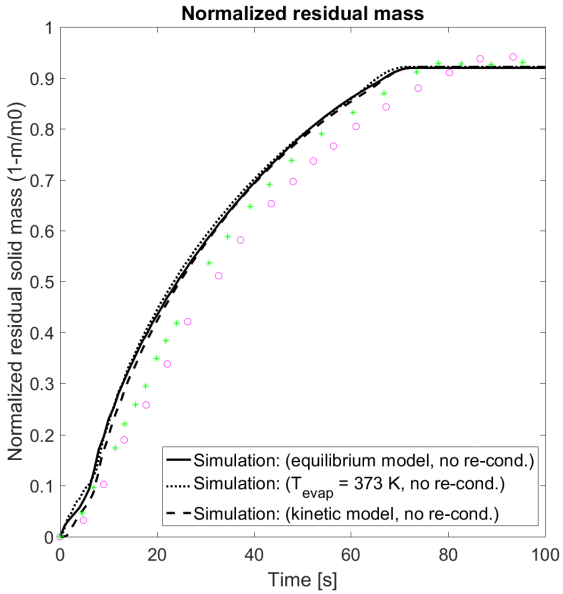

(b) Comparison of the normalized residual solid mass predicted with the thermal, the kinetic rate and the equilibrium model.

Figure 4: Comparison of the results of the thermal, the kinetic rate and the equilibrium model. The kinetic rate model was used with the kinetic data being A $= 5.6 \times 10^8\ s^{-1}$ and $E_{a,evap} = 88$ kJ/mol. For distinct interpretation of the surface and center temperatures in Figure 4a the online version of this article is recommended to be viewed. All experimental data used for validation has been taken from Lu et al.:[5] + ,+, ○ in Figure 4a are the experimentally determined particle surface temperatures. ○, ○ , ○ , * represent the particle center temperatures in Figure 4a. In Figure 4b *, ○ represent the experimentally measured normalized residual solid masses.

One can clearly see that the equilibrium model predicts very different center temperatures compared to both the kinetic rate and the thermal drying model. The surface temperature and the residual solid mass do not differ significantly. However, the results of the equilibrium model differ most significantly from the experiments, and therefore further discussion of model accuracy, stability and efficiency is only done with the more suitable thermal and kinetic rate models, whose results are closer to what has been experimentally observed. The main reason for the difference between the equilibrium model and the two other drying models is most likely that the equilibirum model is developed for low-temperature drying, which is different from the case we tested in this model (see numerical set-up).

4.1 Grid-independence study

Different numbers of grid points have been tested in order to identify the number of grid points that are required to assure grid-independent results. Initially, the model was tested with 55 grid points along the entire wood particle diameter and subsequently 111 grid points were used to generate the 1D mesh. It was found that the model describing drying and devolatilization yields grid-independent solutions already with 55 grid points (see Figure 5a to Figure 5b).

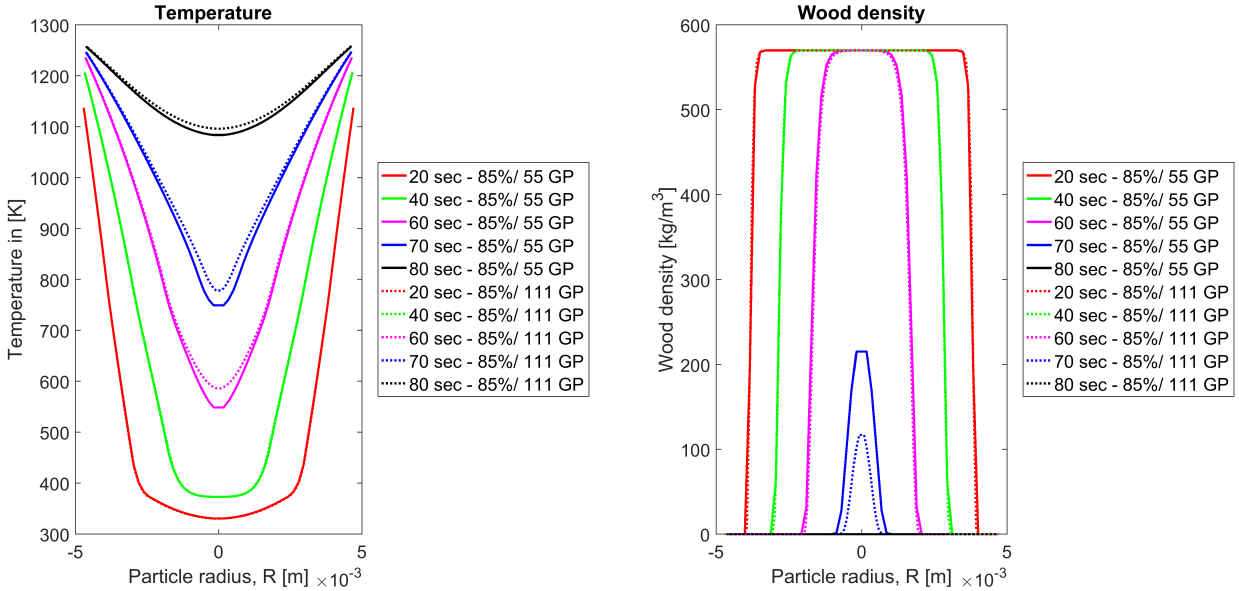

(a) Temperature prediction (thermal drying model with f_{evap}=0.85) with 55 and 111 grid points.

(b) Wood density prediction (thermal drying model with f_{evap}=0.85) with 55 and 111 grid points.

Figure 5: Results of the grid independence study of the thermal drying model with f_{evap}=0.85 and 55 as well as 111 grid points. Re-condensation of water vapor to liquid free water has been considered.

Only the plots for temperature and wood density are shown here. Even though there are some small deviations in the center of the wood particle, the differences are rather minor and do not affect the predicted conversion time. Since predicted values near the particle surface agree well when comparing the coarse and the fine mesh, it is recommended to use the smaller grid point number, since by halving the grid points the CPU time of the drying

and devolatilization model can be significantly decreased. In case of the thermal dyring model with $f_{\text{evap}} = 0.85$, the model with 111 grid points results in a CPU time of 15412 s, which is signicantly larger compared to the same numerical set-up with 55 grid points, where the CPU time is 5045 s.

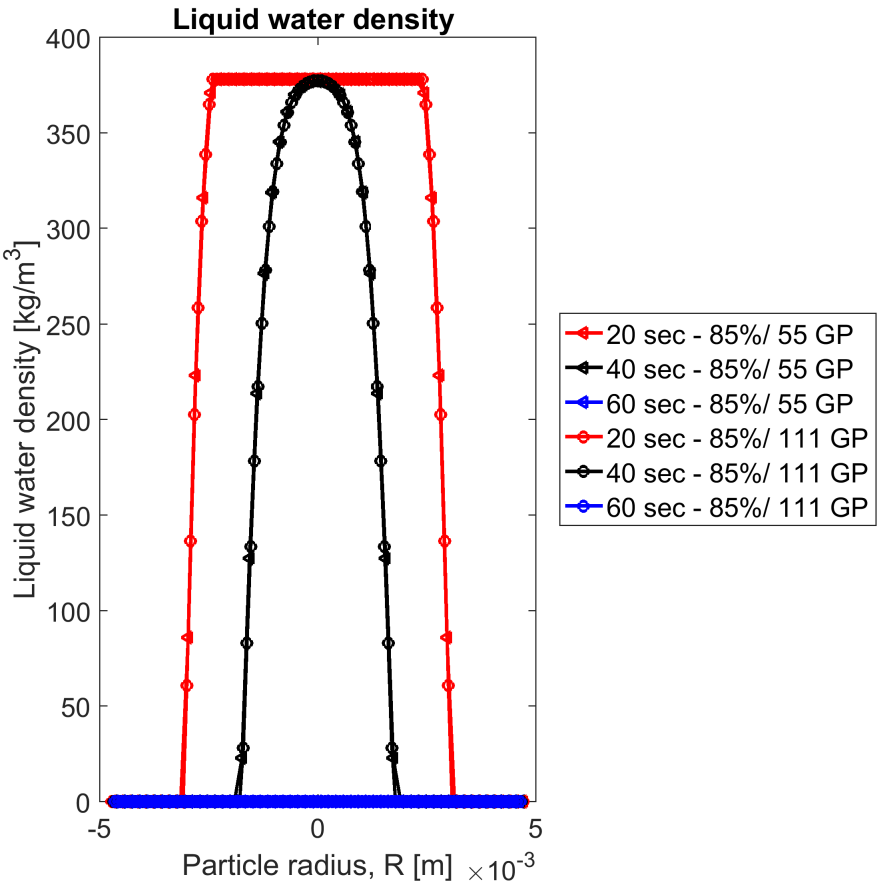

Figure 6: Mesh-independent prediction of drying fronts with the evaporation fraction f_{evap}=0.85. The tested grid point numbers were 55 and 111.

The grid-independence study also showed that the evaporation fraction introduced in this paper, which is smearing the drying fronts predicted with the thermal drying model, is a mesh-independent correction approach for numerical oscillations. Figure 6 shows that the drying fronts of the model run with 55 and 111 grid points overlay each other very nicely, suggesting that the drying front has the same thickness with both the coarse and the fine mesh.

4.2 Numerical instabilities of the thermal drying model

A disadvantage of the thermal drying model is that it tends to give oscillatory numerical results,[9] which can be observed in Figure 7a. The reason behind the oscillations is that as soon as a grid cell that contains water is heated to the evaporation temperature, the entire heat flux to this grid cell is used to evaporate the water. The result of this is that the cell is not heated above the evaporation temperature, which consequently means that the neighboring cell on the cold (and humid) side maintains a temperature *below* the evaporation temperature. When all the water in the evaporating cell is gone, it will therefore take some time before the inferior cell reaches the evaporation temperature. In this period, there is suddenly no evaporation going on. This means that the pressure will be reduced significantly, until the evaporation in the new cell starts and a pressure increase can be observed. This behavior is, however, purely numerical (see Figure 7a and Figure 7b), such that corrections are required.

Yang et al.[6] suggested to overcome these numerical oscillations by multiplying the evaporation rate with a corrective factor. Their correction set-up is the same as the one used in this model, but the assigned corrective factor differs. Yang et al. set the corrective factor equal to 1 if no adjustment of the evaporation term was done, while by setting the corrective factor equal to the initial moisture content (dry basis), the numerical instabilities were reduced.[6] However, we found that if lower moisture contents are to be modeled, this assumption would result in significantly slower drying at one specific location in the wood log or particle, since only a very small fraction of the entire energy theoretically available for drying is then effectively used for evaporation. Consequently, the theoretically thin evaporation zone is significantly smeared out in the model. Therefore, the choice of a more independent corrective factor should result in better agreement with the concept of a sharp-drying front that the thermal drying model is based on.

The correction approach applied in this work was to extend the drying zone over more than one grid point and hereby smear the sharp drying-front, such that the fluctuation

between maximum evaporation rate and minimum evaporation rate (being zero) is avoided. This was achieved by defining the fraction that is reducing the heat flux to a grid cell that could theoretically be used for evaporation in that particular grid cell. The rest of the heat flux is used to heat the cell. A part of this heat will then be conducted further inwards such that eventually also a few of the neighboring grid cells will exceed the evaporation temperature and evaporation of water there will continue simultaneously (see mathematical explanation in Eq. (29)). A higher fraction of heat flux used for heating up the evaporating grid cells, and therefore a lower fraction of heat flux used for evaporation, leads to a larger number of grid points where evaporation occurs simultaneously. This fraction is referred to as evaporation fraction, f_{evap}, in this work. Figure 7b shows how the pressure fluctuations were reduced when applying f_{evap}=0.85.

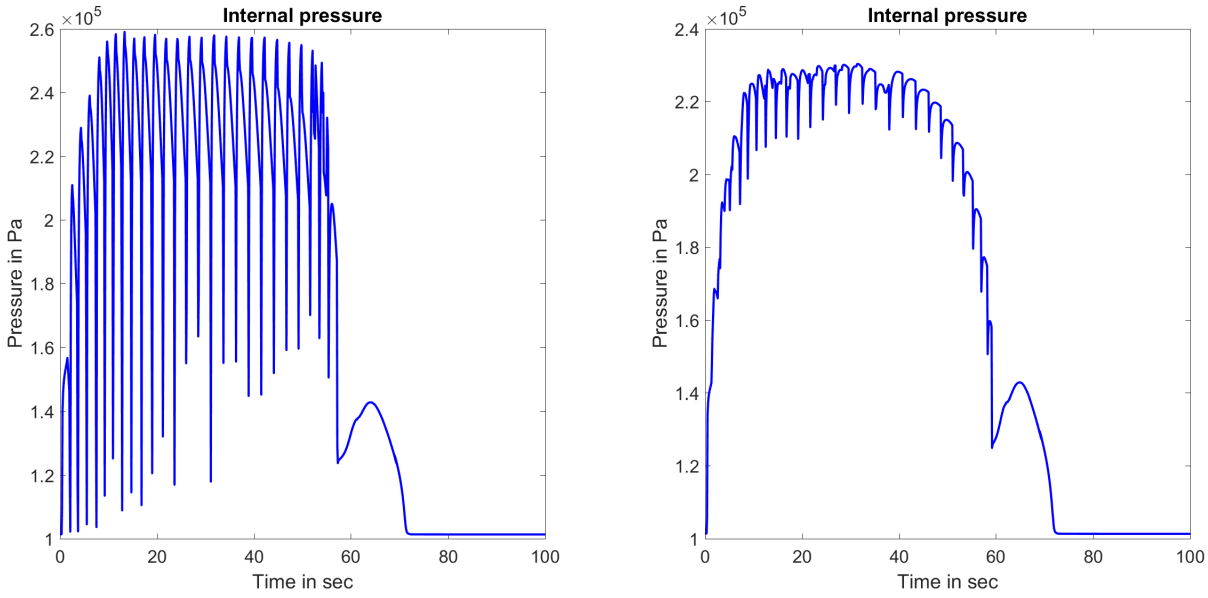

(a) Pressure prediction in the wood particle center (f_{evap}=1).

(b) Pressure prediction in the wood particle center (f_{evap}=0.85).

Figure 7: Internal pressure prediction obtained when applying the thermal drying model without and with correction (f_{evap}=1 or f_{evap}=0.85, respectively). Correction is required to reduce numerical oscillations. Re-condensation of water vapor to liquid free water has been considered.

With f_{evap}=0.85, which expresses that 85% of the incoming heat flux is used for evap-

oration, the pressure oscillations are significantly reduced compared to what is seen when applying f_{evap}=1. In case of f_{evap}=0.85 the drying-front reached over 4 grid points (given at 20 s) (Figure 8a). Therefore, the smearing was still limited, such that the sharp drying-front assumption is still valid. In comparison to f_{evap}=0.85, a lower evaporation fraction (f_{evap}=0.65) led to a more significant smearing over 9 grid points (given at 20 s), as shown in Figure 8b.

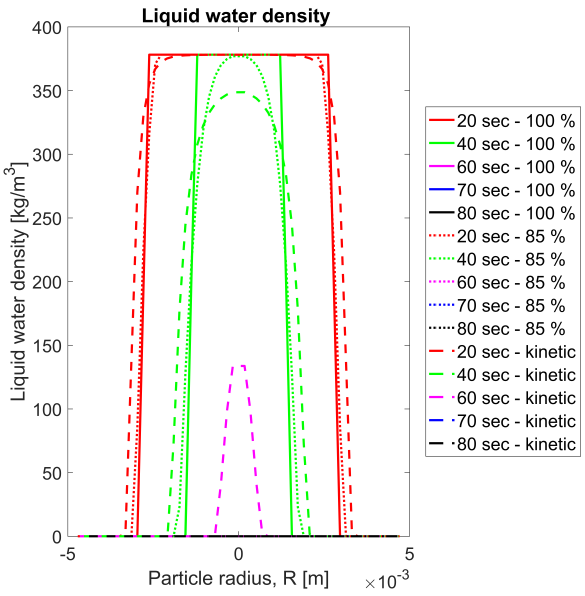

(a) Drying-front at different times for f_{evap}=0.85.

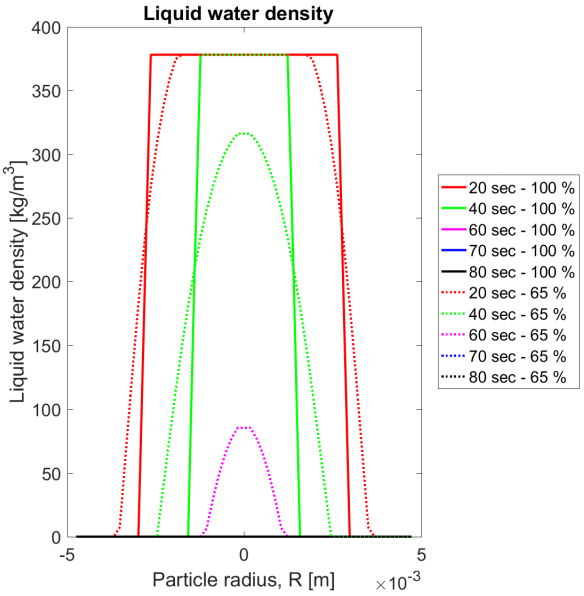

(b) Drying-front at different times for f_{evap}= 0.65.

Figure 8: Comparison of the smearing of the drying-front for f_{evap}=0.85 and f_{evap}=0.65. Both fractions were compared against the non-corrected drying-front, with f_{evap}=1. Re-condensation of water vapor to liquid free water has been considered.

It was found, that a smearing of the drying front over 9 grid points, was too significant with respect to a total number of 27 points along the radius of the wood particle. Such an extensive smearing results in a significant deviation from the modeling concept of a sharp drying-front moving inwards, which is the fundamental idea of the thermal drying model. It is therefore considered inaccurate for the thermal drying model. It was found that applying f_{evap}=0.85 yields more accurate results. Comparing the results of a non-corrected drying-front and a drying-front smeared out by f_{evap} = 0.85 showed that overall the two predictions

agree well (Figure 9 to Figure 12). This confirmed the assumption that $f_{\text{evap}} = 0.85$ can significantly correct the internal pressure fluctuations while at the same time not affecting the model predictions too much. In Figure 8 to Figure 12 "kinetic" refers to a pre-exponential factor of 5.6×10^8 1/s and an activation energy of 88 kJ/mol. Transportation of liquid free water was set to zero, when the thermal model was used.

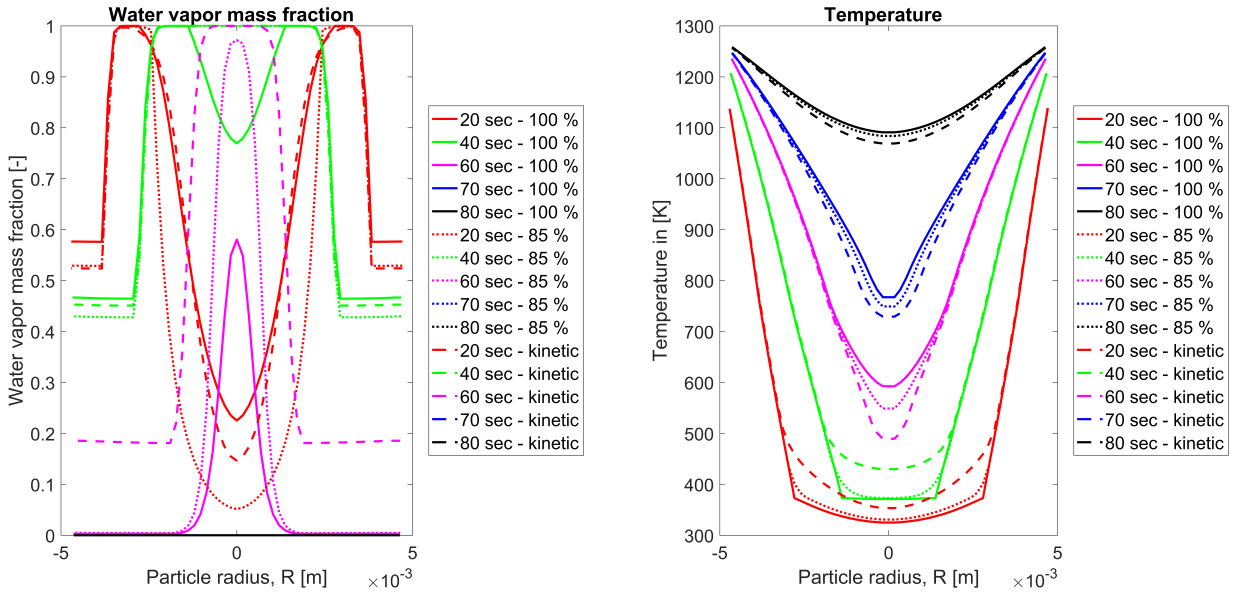

(a) Model results of water vapor mass fraction.

(b) Model results of temperature.

Figure 9: Comparison of water vapor mass fractions and temperature predictions for f_{evap}=0.85 and f_{evap}=1 and the kinetic rate drying model. The initial moisture content was 40 wt% on wet basis and the boiling temperature was fixed to 373 K. Re-condensation of water vapor to liquid free water has been considered.

Significant deviations occur between the corrected thermal drying model (f_{evap}=0.85), the uncorrected thermal drying model (f_{evap}=1) as well as the kinetic rate model when the water vapor mass fraction is modeled (Figure 9a). The kinetic rate model results in different modeling results compared to the thermal model, since it models enhanced drying reactions at higher temperatures than 373 K, such that more time is required to terminate the pre-drying heating. The thermal drying model has meanwhile proceeded slightly further than the kinetic rate drying model at the same time and based on these less enhanced evaporation

reactions, the behavior of the water vapor mass fraction (predicted by the kinetic rate model) follows the behavior of the mass fraction of water vapor predicted by the thermal drying model but is retarded. At 60 s the water vapor mass fractions at the boundaries differ significantly, which is assumed to be due to less enhanced devolatilization reactions in the wood log, when the kinetic rate model is used. This is due to still ongoing evaporation reactions. In contrast to this, the thermal drying model models evaporation reactions to be finished, such that post-drying heating starts earlier, and temperatures where enhanced devolatilization reactions occur are reached earlier. However, at 70 s the water vapor mass fractions predicted by the two drying models result in the same results. At the boundaries the uncorrected and the corrected thermal drying model, do not significantly differ. They predict different results in the particle center as can be seen at 20 s where the deviation is obvious and it is assumed that this is due to enhanced inwards transportation due to diffusion. The uncorrected thermal drying model predicts a high water vapor mass fraction at one specific location, while the inferior grid cell has no evaporation reactions and therefore low water vapor mass fractions. The corrected thermal drying model, however, predicts evaporation reactions at a limited number of neighboring cells and it is assumed that therefore the difference between the mass fractions of water vapor at two neighboring points is lower, such that reduced inwards diffusion occurs. Therefore the mass fraction of water vapor predicted by the uncorrected thermal drying model is highest in the center, which is due to inwards transportation and not due to evaporation reactions. At 60 s it is assumed that reversed effects of diffusion affecting the distribution of water vapor mass fractions cause the discrepancy in modeling results.

The temperature predictions were not significantly affected by the choice of drying model or the application of an evaporation fraction. Deviations can only be detected in the particle center, where both the kinetic rate drying model as well as the corrected thermal drying model (f_{evap}=0.85) resulted in smoother temperature transition between the dry and wet wood zones. However, in the outer particle zones the same temperatures were predicted by

all models.

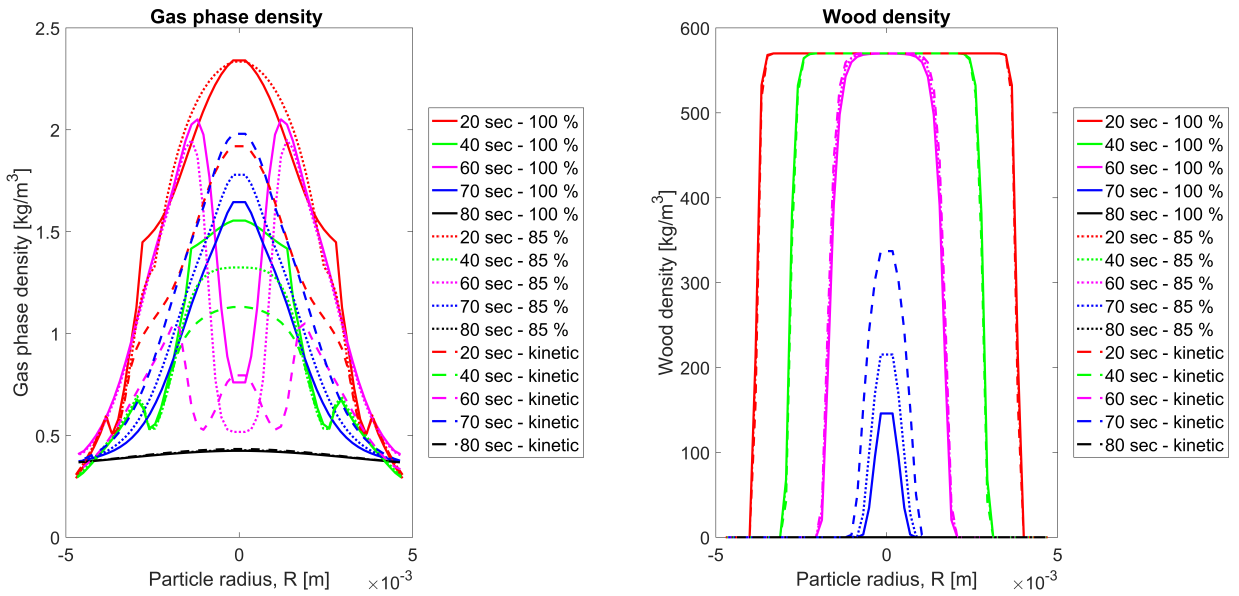

(a) Gas phase density predictions.

(b) Wood density predictions.

Figure 10: Model predictions of total gas density and wood density for f_{evap}=0.85 and f_{evap}=1 and the kinetic rate drying model. The initial moisture content was 40 wt% on wet basis and the boiling temperature was fixed to 373 K. Re-condensation of water vapor to liquid free water has been considered.

The outer peaks of the gas phase density (Figure 10a) are due to devolatilization reactions. When comparing Figure 10a and Figure 10b one can clearly see that the peaks in gas phase density overlap with the zones of dropping wood density. This indicates that the peaks in the gas phase are due to primary devolatilization reactions. Figure 10b shows that the wood density, and therefore also the primary devolatilization modeling results, were not significantly affected by the different drying models, since the deviation between the predictions, clearly visible at 60 s, vanished after 70 s. The difference in gas phase at 60 s is assumed to be mostly due to retarded drying, which was obtained when modeling drying with the kinetic rate drying model. While the kinetic rate drying model still has a peak of gas phase density in the center of the wood particle, which indicates ongoing evaporation reactions, the thermal drying model showed lower values in the center of the particle compared to the devolatilization fronts. This outlines that evaporation reactions

have been terminated in the uncorrected as well as the corrected thermal drying model.

The differences in wood density (Figure 10b) in the center of the particle are rather minor, and are only due to slight differences in evaporation time predictions. This outlines that drying and devolatilization are closely linked and therefore an accurate thermal conversion model has to describe all stages of thermal conversion very well.

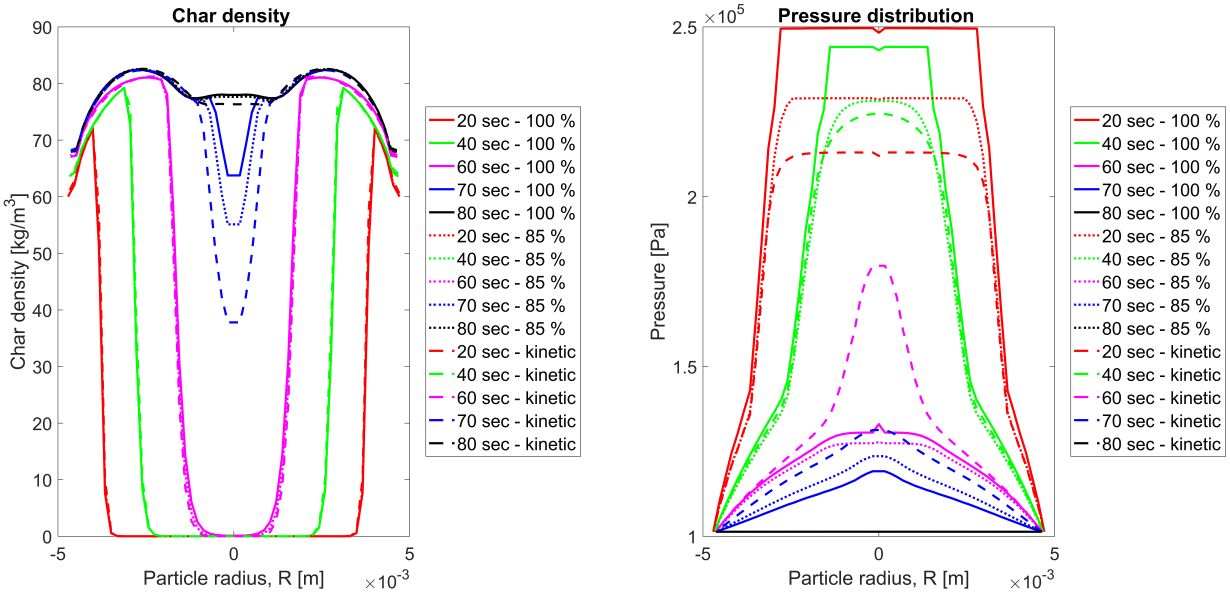

(a) Char density modeling results.

(b) Pressure modeling results.

Figure 11: Model predictions of char density and internal pressure for f_{evap}=0.85 and f_{evap}=1 and the kinetic rate drying model. The initial moisture content was 40 wt% on wet basis and the boiling temperature was fixed to 373 K. Re-condensation of water vapor to liquid free water has been considered.

The internal pressure seems to be affected by the numerical oscillations of the thermal drying model (see Figure 11b). One can clearly see in Figure 11b that a smaller pressure gradient occurs in the zones where the stage of devolatilization has been accomplished. This flattening is due to the increased permeability of the char layer, which enhances the outwards flow of the gas. Here, pressure cannot build up as significantly as in the dry or wet wood areas of the particle, where a lower permeability is given. One can also clearly see that the assumption of different drying models does not affect char densities (Figure 11a) significantly.

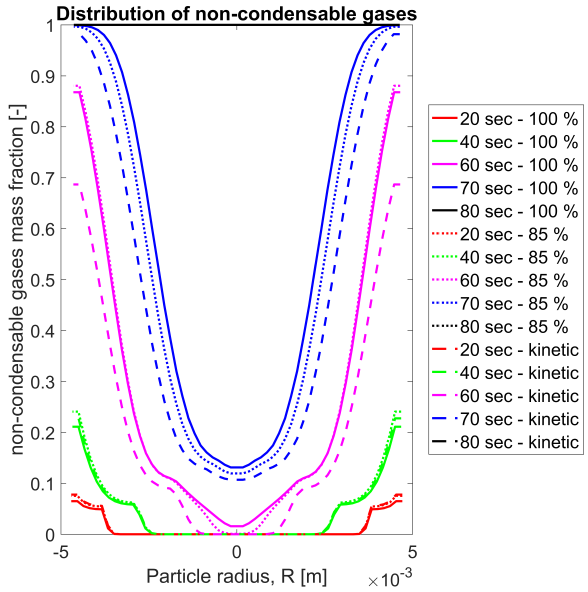

(a) Non-condensable gas species mass fraction modeling results.

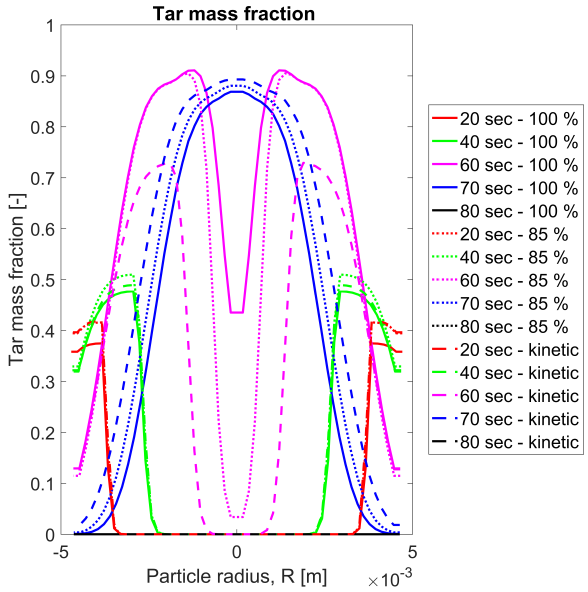

(b) Tar mass fraction modeling results.

Figure 12: Comparison of non-condensable gas species mass fraction and tar mass fraction predictions for f_{evap}=0.85 and f_{evap}=1 and the kinetic rate drying model. The initial moisture content was 40 wt% on wet basis and the boiling temperature was fixed to 373 K. Re-condensation of water vapor to liquid free water has been considered.

Little deviation is seen for the non-condensable gases and tar. The highest deviation was observed at 60 s for the tar. This deviation, however, is again fully balanced at 80 s and at least slightly less significant at 70 s. The differences in tar and non-condensable gas are assumed to be due to the difference in temperature which most likely is due to the retarded drying stage modeled by the kinetic rate drying model and the corrected thermal drying model compared to the uncorrected thermal drying model. It is also interesting to see that, between 70 s and 80 s, ongoing secondary tar reactions lead to complete consumption of tar and a significant increase in non-condensable gases.

The most important finding of this section is that both thermal drying models, corrected by f_{evap}=0.85 or f_{evap}=1, resulted in more or less similar modeling results, especially near the particle surface. The same total conversion times were obtained (meaning similar predictions of normalized residual solid mass), which highlights that both models are accurate and

587 f_{evap}=0.85 does not introduce any significant errors to the model.

588 4.3 Importance of water vapor re-condensation

589 Even though it is assumed that water vapor re-condensation only occurs to a limited extent,
590 it is interesting to see how its consideration or negligence affect model accuracy. The water
591 vapor was only allowed to re-condense back to liquid free water. The evaporation fraction,
592 f_{evap}, of the thermal drying model was set to unity. No bound water was considered.

593 It was found that for this test case the influence of re-condensation reactions is limited,
594 leading to the conclusion that re-condensation reactions of water vapor can be neglected.

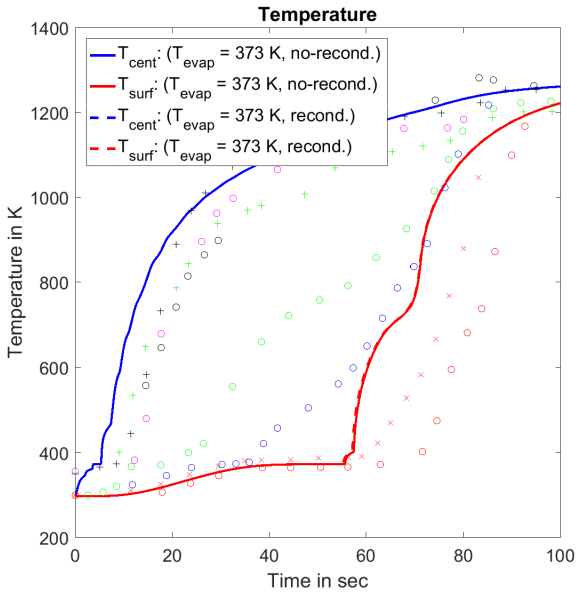

(a) Surface and center temperature modeling results with re-condensation of water vapor and without re-condensation reactions.

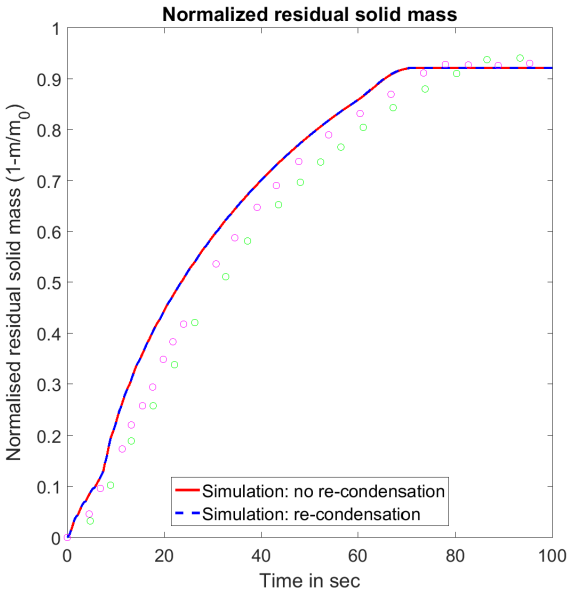

(b) Normalized residual solid mass modeling results with re-condensation of water vapor and without re-condensation reactions.

Figure 13: Comparison of temperature and normalized residual solid mass predictions; once with and once without water vapor re-condensation. The thermal drying model, with an evaporation fraction of 1 and a fixed boiling temperature was applied. The initial moisture content was 40wt% w.b. All experimental data used for validation has been taken from Lu et al.:[5] + ,+, ○ in Figure 13a are the experimentally determined particle surface temperatures. ○, ○ , ○ , * represent the particle center temperatures in Figure 13a. In Figure 13b *, ○ represent the experimentally measured normalized residual solid masses.

As can be seen from Figure 13 there is hardly any difference in modeling results. This suggests that the water vapor re-condensation reactions can as well be neglected. Consequently it is valid to apply the simplifying assumption of negligible re-condensation reactions, without hereby significantly affecting model accuracy.

4.4 Pressure-dependent boiling temperature

The thermal drying model was also tested by using a boiling temperature that is modeled as a function of internal pressure. The accuracy of a pressure-dependent boiling temperature is closely linked to the assumed permeabilities of wood, as the permeabilities define the maximum internal pressure and therefore also the evaporation temperature.

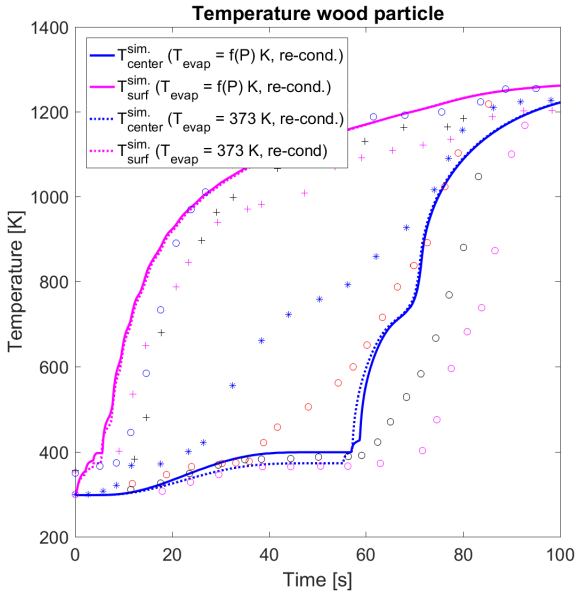

(a) Predicted center and surface temperature (T_{evap} being 373 K and pressure-dependent).

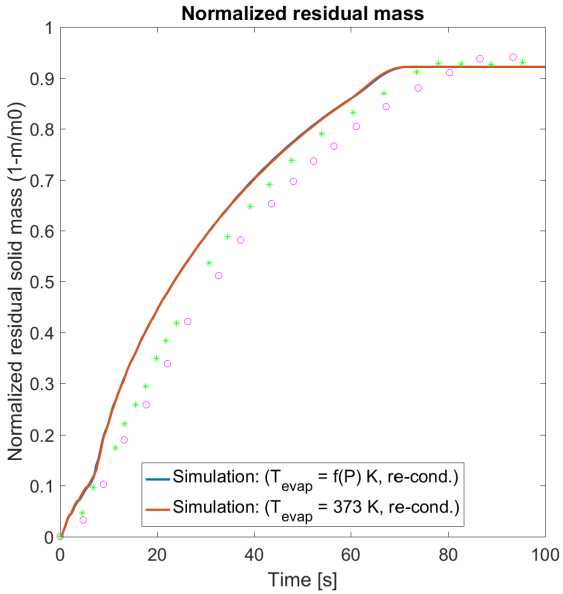

(b) Normalized residual solid mass predicted (T_{evap} being 373 K and pressure-dependent).

Figure 14: Comparison of predictions of normalized residual solid mass and temperatures at the particle surface and in the particle center by first assuming the thermal drying model with a fixed boiling temperature of 373 K and by secondly assuming the thermal drying model with a pressure-dependent boiling temperature. The evaporation fraction was 1 and the initial moisture content was 40 wt% w.b. All experimental data used for validation has been taken from Lu et al.:[5] + ,+, ○ in Figure 14a are the experimentally determined particle surface temperatures. ○, ○ , ○ , * represent the particle center temperatures in Figure 14a. In Figure 14b *, ○ represent the experimentally measured normalized residual solid masses. Re-condensation of water vapor to liquid free water has been considered.

Comparing the modeling results in Figure 14a and Figure 14b of the two different thermal drying modeling approaches shows that the differences in the model predictions are very small, even though one can clearly see that the temperature plateau which is at 373 K for the common thermal drying model with fixed boiling temperature, increased to slightly higher temperature when the boiling temperature was made pressure-dependent (Figure 14a). The predicted surface temperatures are hardly affected. It was found that the predicted normalized residual solid mass was similar for both conepts of the thermal drying model.

On can conclude that assuming a pressure-dependent boiling temperature does not result in a significant increase of accuracy of the model but is rather superfluous for conditions

similar to the ones tested in this model.

4.5 Combined drying model

Even though it has been found that applying the thermal drying model and the kinetic rate drying model separately results in accurate model predictions of drying (Figure 15), it is of interest to identify how model accuracy is affected if the two models are combined. If such a combination of the drying models is done, the kinetic rate model is used to describe bound water evaporation, while the thermal model is used to describe liquid free water evaporation. A combination of drying models is supposed to mimic that liquid free water and bound water evaporate differently.

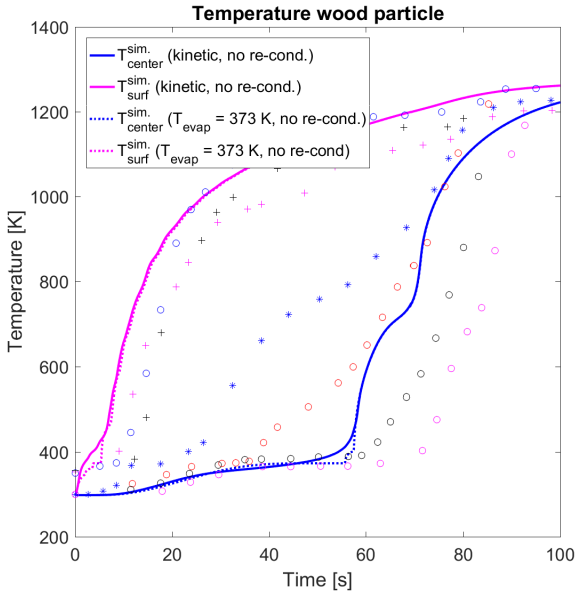

(a) Predicted center and surface temperature predicted when applying the kinetic rate drying model compared to the thermal model.

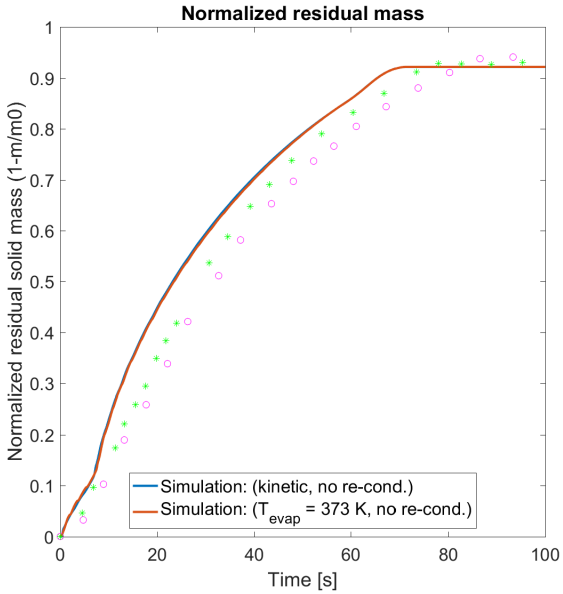

(b) Normalized residual solid mass predicted when applying the kinetic rate drying model compared to the thermal model.

Figure 15: Comparison of predictions of normalized residual solid mass and temperatures at the particle surface and in the particle center by assuming the thermal drying model with a fixed boiling temperature or by assuming the kinetic rate drying model with a high pre-exponential factor (A: 5.13 $\times$ 10^{10} 1/s and E_a: 88 kJ/mol). The kinetic drying model was compared against the thermal drying model with the evaporation fraction being 1. Re-condensation of water vapor to liquid free water has not been considered when describing evaporation of by the thermal drying model (=dotted lines). The initial moisture content of 40 wt% w.b. All experimental data used for validation has been taken from Lu et al.:[5] + ,+, ∘ in Figure 15a are the experimentally determined particle surface temperatures. ∘, ∘ , ∘ , * represent the particle center temperatures in Figure 15a. In Figure 15b *, ∘ represent the experimentally measured normalized residual solid masses.

The applied kinetic data in Figure 15a and Figure 15b were based on a high pre-exponential factor and therefore a very fast drying process, which involves only a few grid points at the same time. One can see that there is hardly any difference in the predictions when using the thermal drying model and the kinetic rate drying model separately. The kinetic data with a lower pre-exponential factor (A: 5.6 $\times$ 10^8 1/s and E_a: 88 kJ/mol) showed significant deviation from thermal drying model predictions regarding the prediction of the center temperature, as shown in Figure 16.

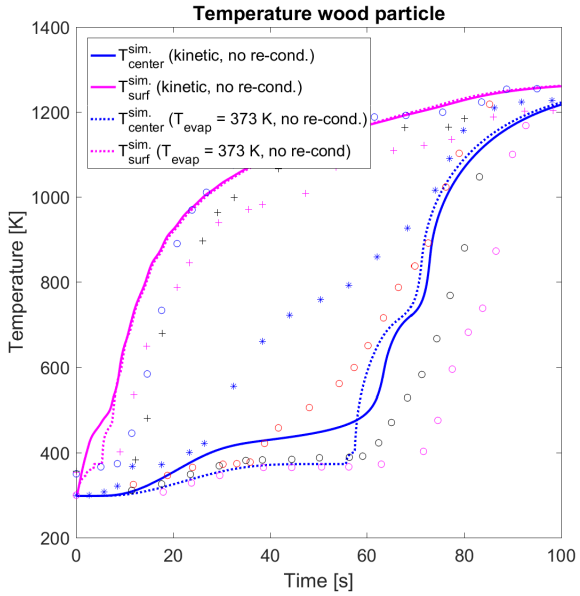

Figure 16: Predicted temperatures at the particle surface and in the particle center by assuming the kinetic rate drying model with a lower pre-exponential factor (A: 5.6×10^8 1/s and E_a: 88 kJ/mol). The kinetic drying model was compared against the thermal drying model results, with the evaporation fraction being 1. Re-condensation of water vapor to liquid free water has not been considered when using the thermal drying model (=dashed lines). The initial moisture content was 40 wt% w.b. Experimental results for validation were taken from Lu et al.[5] and the correlating markings of experimental data are: $T_{surface}$: ○ , +, + ; T_{center}: ○ , ○, ○ , ∗ .

When testing a combined drying model a numerical set-up with total liquid water content being split into bound water and liquid free water by the fiber saturation point M_{fsp} (30 wt% moisture content on oven-dry basis) was used. The evolution of these two types of liquid water, can be seen in Figure 17. The boiling temperature was assumed to be 373 K. The applied kinetic rate drying model was based on a pre-exponential factor of 5.6×10^8 1/s and an activation energy of 88 kJ/mol.

It was found that modeling the present liquid water as a combination of bound water and liquid free water did not increase the accuracy of the model. The accuracy of normalized residual solid mass and surface as well as center temperature predictions could not be increased.

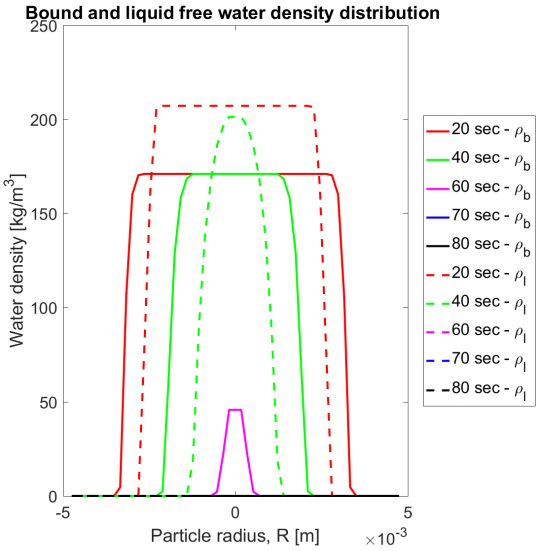

Figure 17: Water densities of liquid free water (ρ_l) and bound water (ρ_b) along the wood particle diameter plotted at different times.

It is assumed that the most important aspect of an accurate drying model is an accurate description of the evaporation, while the description of liquid water transportation does not significantly influence the modeling results. However, it has to be mentioned that in the test cases discussed in this paper, high-temperature drying conditions are given, such as in a wood stove. Liquid water transportation might become more important if low-temperature drying processes are modeled.

4.6 Numerical efficiency of the drying models

In order to evaluate numerical efficiency of the drying models, the CPU times were compared (see Table 4).

Table 4: CPU times of different drying models. "TDM" is the abbreviation for the *"Thermal drying model"* and "KRDM" is the abbreviation for the *"Kinetic rate drying model"*. f(P) indicates that the boiling temperature was modeled as a function of the internal pressure.[1)] marks that the thermal drying model is considering re-condensation reactions of water vapor to liquid free water. The final time used in this test cases was always 100 s.

Drying model	T_{evap} [K]	A_{evap} [1/s]	$E_{a,\ evap}$ [kJ/mol]	Evaporation fraction, f_{evap} [-]	M_{water} [wt% w.b.]	CPU time [s]
TDM[1)]	373	-	-	0.65	40	3415
TDM[1)]	373	-	-	0.85	40	3685
TDM[1)]	373	-	-	1	40	5045
TDM[1)]	f(P)	-	-	0.85	40	3334
TDM[1)]	f(P)	-	-	1	40	4309
KRDM	-	5.6×10^8	88	-	40	3467
KRDM	-	5.13×10^{10}	88	-	40	2930
TDM[1)] & KRDM	f(P)	5.6×10^8	88	0.85	40	3947

It can clearly be seen that the model requires more time to reach convergence, if the thermal drying model is used without the evaporation fraction. It is assumed that the reason is that in the uncorrected drying model significant fluctuations of the internal pressure have to be modeled. When smearing the sharp drying-front by an evaporation fraction of 0.65 the CPU time decreases from 5045 s to 3415 s, while the CPU time decreased slightly less (to 3685 s) when applying an evaporation fraction of 0.85. Hence, the evaporation fraction does not only reduce numerical oscillations but also affects numerical efficiency of the model. It was also found that modeling a pressure-dependent boiling temperature for the thermal drying model resulted in reduced CPU times. With a fixed boiling temperature the CPU time was 5045 s, while it was 4309 s when modeling a pressure-dependent boiling temperature. In both cases the drying-front was not smeared (evaporation fraction being unity).

Kinetic rate drying models, which are considered more numerically stable, are more numerically efficient compared to the thermal drying models. By increasing the pre-exponential factor of the Arrhenius term describing evaporation, enhanced evaporation is shifted to lower temperatures. For a pre-exponential factor of the order of $10^8\ s^{-1}$ the CPU time is as high as 3467 s and it is therefore faster than the uncorrected thermal drying model (5045 s). By further increasing the pre-exponential factor from $5.6 \times 10^8\ s^{-1}$ to $5.13 \times 10^{10}\ s^{-1}$ the CPU

time dropped to 2930 s.

The combined drying model resulted in a CPU time that was in the range of the separate corrected thermal drying model ($f_{\text{evap}} = 0.85$), as can be seen from Table 4.

Numerical efficiency of the thermal drying model can be improved by applying evaporation fractions and hereby smearing the drying front. Nonetheless, it has to be pointed out that the choice of evaporation fraction cannot be done arbitrarily with the sole purpose of reducing oscillatory numerical results and CPU times. One has to also consider that evaporation fractions cannot be chosen too small, since they will also have an effect on model accuracy.

5 Conclusions and recommendations

In this work, the numerical instabilities of the thermal drying model, the accuracy of the thermal drying model and the kinetic rate drying model as well as the numerical efficiency of the two models were investigated. In order to accomplish this a 1D mesh-based drying and devolatilization model was developed.

It was found that re-condensation reactions do not have to be modeled, since they do not increase model accuracy. Neglecting re-condensation of water vapor has proven to be a valid simplifying assumption.

The sensitivity of modeling results to the liquid permeability was investigated. It was shown that, with respect to thermal wood conversion applications similar to wood stoves, where lower moisture contents of wood are critical for the stove's operation, one can neglect the liquid free water convection. This is due to the rather low effective permeabilities of the liquid water, which lead to similar results as a model that is fully neglecting liquid free water convection.

It was found that the thermal drying model resulted in oscillatory numerical solutions that require correction. Therefore, an evaporation fraction was introduced, that smeared the

drying-front, such that evaporation was numerically allowed to occur at a limited number of neighboring grid points. Hereby, the oscillations, clearly visible when plotting the internal pressure evolution, were reduced and more physically reasonable results were obtained.

Furthermore, it was found that, at least for the small thermally thick wood particles, tested in this work, there is no significant difference between assuming a fixed boiling temperature or a pressure-dependent boiling temperature.

Applying a combined model did not improve model accuracy in comparison to separately applied kinetic rate drying models or thermal drying models.

Numerical efficiency tests showed that a corrected thermal drying model with an evaporation fraction of 0.85 operates at lower computational cost than the uncorrected thermal drying model. The pressure-dependent boiling temperature assumption also resulted in reduced CPU time. When applying the kinetic rate model with a higher pre-exponential factor the CPU times were reduced compared to the kinetic rate drying model with lower pre-exponential factors.

6 Acknowledgments

This work has been carried out within the WoodCFD (243752/E20) project, which is funded by: Dovre AS, Norsk Kleber AS, Jøtulgruppen and Morsø AS together with the Research Council of Norway through the ENERGIX program.

References

(1) Porteiro, J.; Granada, E.; Collazo, J.; Patiño, D.; Morán, J. C. *Energy Fuels* **2007**, *21*, 3151–3159.

(2) Porteiro, J.; Míguez, J. L.; Granada, E.; Moran, J. C. *Fuel Process. Technol.* **2006**, *87*, 169–175.

(3) Thunman, H.; Leckner, B.; Niklasson, F.; Johnsson, F. *Combust. Flame* **2002**, *129*, 30–46.

(4) Mehrabian, R.; Zahirovic, S.; Scharler, R.; Obernberger, I.; Kleditzsch, S.; Wirtz, S.; Scherer, V.; Lu, H.; Baxter, L. L. *Fuel Process. Technol.* **2012**, *95*, 96 – 108.

(5) Lu, H.; Robert, W.; Peirce, G.; Ripa, B.; Baxter, L. L. *Energy Fuels* **2008**, *22*, 2826–2839.

(6) Yang, Y. B.; Sharifi, V. N.; Swithenbank, J.; Ma, L.; Darvell, L. I.; Jones, J. M.; Pourkashanian, M.; Williams, A. *Energy Fuels* **2008**, *22*, 306–316.

(7) Kwiatkowski, K.; Bajer, K.; Celińska, A.; Dudyński, M.; Korotko, J.; Sosnowska, M. *Fuel* **2014**, *132*, 125–134.

(8) Skreiberg, Ø.; Seljeskog, M.; Georges, L. *Chemical Engineering Transactions* **2015**, *43*, 433– 438.

(9) Fatehi, H.; Bai, X. S. *Combust. Sci. Technol.* **2014**, *186*, 574–593.

(10) Haberle, I.; Skreiberg, Ø.; Łazar, J.; Haugen, N. E. L. *Prog. Energy Combust. Sci.* **2017**, *63*, 204 – 252.

(11) Galgano, A.; Di Blasi, C. *Combust. Flame* **2004**, *139*, 16 – 27.

(12) Galgano, A.; Di Blasi, C. *Ind. Eng. Chem. Res.* **2003**, *42*, 2101–2111.

(13) Di Blasi, C. *Int. J. Heat Mass Transfer* **1998**, *41*, 4139 – 4150.

(14) Di Blasi, C. *Chem. Eng. Sci.* **1996**, *51*, 1121 – 1132.

(15) Biswas, A. K.; Umeki, K. *Chem. Eng. J.* **2015**, *274*, 181 – 191.

(16) Larfeldt, J.; Leckner, B.; Melaaen, M. C. *Fuel* **2000**, *79*, 1637–1643.

(17) Ström, H.; Thunman, H. *Combust. Flame* **2013**, *160*, 417 – 431.

(18) Van de Velden, M.; Baeyens, J.; Brems, A.; Janssens, B.; Dewil, R. *Renewable Energy* **2010**, *35*, 232 – 242.

(19) Neves, D.; Thunman, H.; Matos, A.; Tarelho, L.; Gómez-Barea, A. *Prog. Energy Combust. SCi.* **2011**, *37*, 611 – 630.

(20) Rath, J.; Wolfinger, M.; Steiner, G.; Krammer, G.; Barontini, F.; Cozzani, V. *Fuel* **2003**, *82*, 81 – 91.

(21) Grønli, M. G. A theoretical and experimental study of thermal degradation of biomass. PhD thesis, Norwegian University of Science and Technology, Trondheim, 1996.

(22) de Paiva Souza, M. E.; Nebra, S. A. *Wood and Fiber Science* **2000**, *32*, 153–163.

(23) Spolek, G. A.; Plumb, O. A. *Wood Science and Technology* **1981**, *15*, 189–199.

(24) Tesoro, F. O.; Choong, E. T.; Kimbler, O. K. *Wood and Fiber Science* **1974**, *6*, 226–236.

(25) Raznjevic, K. *Handbook of Thermodynamic Tables and Charts*; Hemisphere Publishing Corporation: Washington, 1976; pp 1–392.

(26) Siau, J. F. *Wood Sci.* **1980**, *13*, 11 – 13.

(27) Stamm, A. J. *Wood and Cellulose Science*; Ronald Press: New York, 1964; pp 1–549.

(28) National Laboratory Lawrence Livermore, SUNDIALS: SUite of Nonlinear and DIfferential/ALgebraic Equation Solvers - IDA. 2016; http://computation.llnl.gov/projects/sundials/ida [accessed 2017-04-07].

(29) Ouelhazi, N.; Arnaud, G.; Fohr, J. P. *Transp. Porous Media* **1992**, *7*, 39–61.

(30) Bryden, K. M.; Hagge, M. J. *Fuel* **2003**, *82*, 1633 – 1644.

(31) Peters, B.; Bruch, C. *J. Anal. Appl. Pyrolysis* **2003**, *70*, 233 – 250.

(32) Di Blasi, C.; Branca, C.; Sparano, S.; Mantia, B. L. *Biomass Bioenergy* **2003**, *25*, 45 – 58.

(33) Chan, W.-C. R.; Kelbon, M.; Krieger, B. B. *Fuel* **1985**, *64*, 1505–1513.

(34) Wagenaar, B.; Prins, W.; van Swaaij, W. *Fuel Process. Technol.* **1993**, *36*, 291 – 298.

(35) Liden, A.; Berruti, F.; Scott, D. *Chem. Eng. Commun.* **1988**, *65*, 207–221.

(36) Koufopanos, C.; Papayannakos, N.; Maschio, G.; Lucchesi, A. *Can. J. Chem. Eng.* **1991**, *69*, 907–915.

(37) Di Blasi, C. *Combust. Sci. Technol.* **1993**, *90*, 315–340.

(38) Forest Products Laboratory, *Wood Handbook - Wood as an Engineering Material. General Technical Report FPL–GTR–190*; U.S. Department of Agriculture: Madison, Wisconsin, 1999.

(39) Pozzobon, V.; Salvador, S.; Bézian, J. J.; El-Hafi, M.; Maoult, Y. L.; Flamant, G. *Fuel Process. Technol.* **2014**, *128*, 319 – 330.

(40) Hagge, M. J.; Bryden, K. M. *Chem. Eng. Sci.* **2002**, *57*, 2811 – 2823.

(41) Park, W. C.; Atreya, A.; Baum, H. R. *Combust. Flame* **2010**, *157*, 481 – 494.